energies

MDPI

Article

Parametric CFD Analysis of Annular Groove Geometry on Nucleation Dynamics and Thermal Resistance in Thermosyphon Heat Pipes

Shek Mohammod Atiqure Rahman [1,2,*], Salah Issa [2,3], Essam M. Abo Zahhad [4,5], Ahmed Amine Hachicha [1,2], Mamdouh El Haj Assad [1,2], Md Hasanuzzaman [6] and Ali Mohammed Radwan [1]

[1] Department of Sustainable and Renewable Energy Engineering, University of Sharjah, Sharjah P.O. Box 27272, United Arab Emirates; ahachicha@sharjah.ac.ae (A.A.H.); massad@sharjah.ac.ae (M.E.H.A.); ali.radwan@sharjah.ac.ae (A.M.R.)
[2] Sustainable Energy Development Research Group, Sustainable Energy and Power, Systems Research Center, Research Institute for Sciences and Engineering, University of Sharjah, Sharjah P.O. Box 27272, United Arab Emirates; salah.elsayed1@student.unimelb.edu.au
[3] Department of Infrastructure Engineering, Faculty of Engineering and Information Technology (FEIT), University of Melbourne, Melbourne 3053, Australia
[4] Department of Mechanical and Industrial Engineering, Liwa College, Abu Dhabi P.O. Box 41009, United Arab Emirates; essam.mohamed@lu.ac.ae
[5] Mechanical Power Engineering Department, Faculty of Energy Engineering, Aswan University, Aswan 81528, Egypt
[6] Higher Institution Centre of Excellence (HICoE), UM Power Energy Dedicated Advanced Centre (UMPEDAC), Level 4, Wisma R&D, Universiti Malaya, Jalan Pantai Baharu, Kuala Lumpur 59990, Malaysia; hasan@um.edu.my
* Correspondence: srahman@sharjah.ac.ae

Abstract

Annular grooves are widely proposed as a passive enhancement for two-phase closed thermosyphons, yet the literature reports their effect almost exclusively through global thermal metrics, leaving the underlying vapor-generation and vapor-retention mechanisms largely unquantified. This study makes three contributions: it quantifies, from resolved vapor fields, the link between annular groove geometry and local vapor-generation behavior; it identifies the competing influence of groove-enhanced vapor generation against groove-induced vapor retention within a single computational framework; and it identifies the best of the tested groove spacing-to-width combinations. A transient two-dimensional volume-of-fluid model, closed by a temperature-driven Lee-type user-defined function for evaporation and condensation, was developed for a water-charged copper thermosyphon at two heat inputs, 81 W and 101 W. The smooth-wall model was validated against published experimental wall temperatures with a mean deviation of 4.15% (maximum about 5.7% at the condenser end); the grooved cases were assessed through trend comparison with grooved and corrugated thermosyphon studies. Groove spacing was varied between 2.5, 5.0 and 10.0 mm (width 1.0 mm), and groove width between 0.5, 1.0 and 1.5 mm (spacing 5 mm). Grooves lowered the peak (hot-spot) wall temperature by 2.6 K at 81 W and 4.3 K at 101 W and raised the evaporator vapor fraction by about 12–19%; widening the grooves from 1.0 to 1.5 mm increased the number of active vapor sites by about 19%. Reducing the groove spacing promoted earlier and more frequent vapor release, whereas increasing the groove width raised vapor generation but prolonged vapor residence. The overall thermal resistance of the grooved pipe was slightly higher than that of the smooth pipe (by about 1.4% at 81 W and 2.2% at 101 W), so the local gains do not automatically give lower overall resistance. The best tested combination was S = 5 mm and W = 1.0 mm (S/W = 5); the thermal resistance of the five simulated groove combinations differed by only about 0.5%. The results provide comparative design guidance for grooved thermosyphons.:

Check for updates

Academic Editor: Zhang Jianfei

Received: 17 October 2026
Revised: 17 November 2026
Accepted: 21 November 2026
Published: 27 November 2026

Copyright: © 2026 by the authors. Licensee MDPI, Basel, Switzerland. This article is an open access article distributed under the terms and conditions of the Creative Commons Attribution (CC BY) license.

Keywords: thermosyphon heat pipes; annular grooves; CFD; bubble dynamics; thermal resistance

1. Introduction

The shift towards renewable energy is essential for meeting future energy demands and addressing climate challenges. Key technologies in the renewable energy sector include solar photovoltaic systems, wind turbines, hydropower, and solar thermal systems. Among these technologies, solar thermal systems are particularly prevalent because they efficiently convert abundant and renewable solar energy into heat [1]. Furthermore, solar thermal systems offer a scalable and cost-effective solution for high-temperature applications such as industrial processes [2], water heating, space heating and electricity generation through thermal power plants. Furthermore, the capacity for thermal energy storage enhances the reliability of solar thermal systems by enabling energy use even during periods of low sunlight [3]. Solar collectors are central to solar thermal systems, capturing solar energy and converting it into usable heat. Among the various types, Evacuated Solar Collectors (ESCs) are notable for their high efficiency and adaptability, using vacuum-insulated tubes to reduce heat loss and enhance thermal performance [4]. Generally, ESCs are widely used for domestic hot water supply and heating applications, including heat pipe and U-tube glass Evacuated Tube Solar Collectors (ETSCs), which are more commonly used than heat pipe collectors [5]. However, heat pipe-based ETSCs offer extra advantages, such as rapid start-up, high-pressure resistance, and ease of installation and maintenance. Hence, pipe-based ETSCs have attracted the attention of many researchers [6]. As the heat pipes are boosted, ETSC's thermal efficiency improves. U-tube or natural-circulation flow ETSCs are single-phase devices that capitalize on sensible heating. Liu and Zhang [7] conducted an experimental study on the thermal response of walls with implanted heat pipes. Zhang et al. [8] demonstrated the temperature distribution characteristics and energy-saving potential of a wall implanted with heat pipes during the heating season. In contrast, heat pipe ETSCs are multi-phase systems that utilize sensible and latent heat transfer. It is worth mentioning that the multi-phase system is 42.8% more effective than the single-phase system [9]. In the existing literature, considerable research and development efforts have focused on improving the heat-transfer performance of heat pipes and minimizing thermal resistance. The heat pipes are employed in ETSC and for various applications [10,11]. Extensive research has examined the thermal performance of heat pipes under varying operating parameters, such as fill ratios [12], inclination angles, and working fluids. Many researchers have extensively used Computational Fluid Dynamics (CFD) simulations to explore the complex interactions between design parameters and thermal performance [13–15]. Alammar et al. [16] used CFD to study the impact of fill ratio and inclination angle on the thermal performance of a thermosyphon heat pipe. CFD model results closely matched experimental data, with a maximum discrepancy of 4.2% in the temperature distribution, 8.1% in thermal resistance, and 1.3% in the inclination angle. Al Jubouri and Jawad [17] conducted a computational evaluation using CFD to analyze the thermal behavior of a heat pipe under several conditions. The key findings revealed that increasing the heat input reduced thermal resistance and that the filling ratio had a pronounced effect on the evaporator wall temperature, especially at higher heat input. Yue et al. [18] used CFD simulations to study heat transfer and flow mechanisms in a Microchannel Separate Heat Pipe (MCSHP) under varying filling ratios, focusing on the evaporator used for cooling in environments like telecommunication stations. The optimal refrigerant filling ratio for the MCSHP was determined to be between 68% and 100%. Furthermore, Höhne [19] used CFD simulations with a homogeneous model and a modified Lee model to study heat and

mass transfer in heat pipes during evaporation and condensation. Previous CFD studies by Maghrabie et al. [20] Kalogirou & Papamarcou [21] examined multiphase modeling and thermosyphon systems but overlooked the influence of annular groove geometry.

In recent years, substantial research has been devoted to improving the thermal efficiency of heat pipes by modifying internal geometries [22–25], particularly through the introduction of grooves [26–28] that enhance nucleation and bubble dynamics under two-phase flow conditions. Wang [29] investigated bent heat pipes with grooved surfaces and found that tailored groove geometries significantly enhance boiling initiation, thereby reducing thermal resistance and improving vapor transport [29]. Moreover, broader studies on grooved channel flows, such as the turbulent-flow simulation of periodic grooves of varying corner curvature by Mukherjee et al. [30], reported that rounding the groove corners raised the Nusselt number by about 12% for Re = 6000–36,000. This indicates that groove geometry, including corner shape, influences convective heat transfer in single-phase channels as well as in heat pipes. An emerging frontier in heat pipe research lies in modifying heat pipes with annulus grooves [31,32]. Strategically integrated into the heat pipe structure, these grooves enhance heat-transfer efficiency and reduce thermal resistance [31–33]. These grooves enhance thermal performance by augmenting the available surface area for heat transfer [34–36]. Groove modifications have multiple potential benefits in heat pipes. Heat pipes with annular grooves facilitate more efficient heat transfer by increasing the surface area. This leads to augmented energy efficiency and heightened system performance. Notwithstanding the wealth of research on heat pipe technology, computational fluid dynamics simulations of heat pipes modified with annular grooves remain relatively scarce.

Table 1 also summarises the domain, turbulence treatment and phase-change model of each study as far as they are stated in the sources consulted ("Not stated" means that the abstract or summary of the source does not say). Where reported, the CFD studies use VOF with a temperature-driven or Lee-type closure, and the domains are two- or three-dimensional; the turbulence treatment is rarely stated for the heat-pipe studies.

Table 1. Summary of representative previous studies.

Reference	Approach	Parameters Studied	Domain	Turbulence	Phase-Change Model	Principal Finding
Alammar et al. [16]	Numerical (CFD, VOF)	Fill ratio; inclination angle	2-D (planar or axisymmetric not stated)	Not stated	Source terms after De Schepper et al., coefficient 0.1 s^{-1}	Maximum deviation 4.2% in temperature, 8.1% in thermal resistance
Al Jubouri and Jawad [17]	Numerical (CFD)	Heat input; filling ratio	2-D	Not stated	Not stated	Thermal resistance falls with increasing heat input
Yue et al. [18]	Numerical (CFD)	Filling ratio, microchannel separate heat pipe	Not stated	Not stated	Not stated	Optimum refrigerant filling ratio 68–100%
Höhne [19]	Numerical (homogeneous + modified Lee)	Evaporation and condensation closure	3-D	Not stated	Homogeneous model, Lee-inspired closure	Demonstrated Lee-type closure for heat pipe phase change
Fadhl et al. [37]	Numerical (VOF + UDF) and experimental	Axial temperature distribution	2-D	Not stated	Temperature-driven UDF (De Schepper-type source terms)	Established the temperature-driven source-term formulation adopted here

Table 1. *Cont.*

Reference	Approach	Parameters Studied	Domain	Turbulence	Phase-Change Model	Principal Finding
Wang et al. [29]	Experimental	Groove geometry in bent heat pipes	–	–	–	Tailored grooves lower thermal resistance and improve vapour transport
Mukherjee et al. [30]	Numerical	Groove corner curvature in a channel (Re = 6000–36,000)	Channel with periodic rectangular grooves	RANS (RNG k–ε in the preprint version)	– (single-phase)	Corner curvature raised the Nusselt number by about 12%
Saygan et al. [31]	Numerical and experimental	Bifurcated groove structure	Reduced-order model (not CFD)	–	–	Capillary boosting improves heat pipe performance
Zhou et al. [28]	Experimental	Large-diameter flattened heat pipes	–	–	–	Improved heat transfer in flattened geometries
Wang et al. [38]	Experimental and numerical (VOF)	Corrugated evaporator	Not stated	Not stated	VOF (closure not stated)	Minimum total thermal resistance 0.0243 K W^{-1}
Magnabosco [39]	Numerical (3D VOF)	Fin cross-sectional shape; working fluid	3-D	Not stated	Not stated (VOF)	Fin geometry governs condensate drainage and condensation performance

Although numerous studies have explored the use of grooved or textured surfaces in heat pipes, several critical gaps remain unaddressed. First, most existing investigations focus on overall thermal performance or provide qualitative descriptions of boiling behavior, without systematically quantifying the effects of annular groove spacing and width on key nucleation parameters, such as nucleation superheat, nucleation site density, bubble residence time, and vapor generation rate. Second, temperature-driven phase-change closures have been applied to smooth thermosyphons [19,37], but the coupled influence of groove geometry and localized evaporation–condensation dynamics in annular-grooved thermosyphon heat pipes has not been quantified. Third, to the best of our knowledge, no prior research has proposed a best spacing-to-width (S/W) ratio for annular grooves based on a detailed analysis of nucleation dynamics and thermal resistance.

The novelty of this study lies in establishing a direct, quantitative link between annular groove geometry and microscale boiling dynamics in thermosyphon heat pipes using a physics-based CFD framework. Unlike prior studies that primarily report global thermal performance or rely on qualitative observations, this work extracts, from the resolved volume-of-fluid fields, the wall superheat at the onset of vapor generation, the number of wall-attached vapor sites, the vapor residence time, and the local vapor-generation rate as functions of groove spacing and width. The Lee-type closure contains no sub-grid nucleation-site model, so these metrics describe grid-resolved vapor structures and are not physical nucleation-site densities.

A second contribution is the use of a temperature-driven phase-change source term within a multiphase CFD model via a user-defined function, following Fadhl et al. [37]. The closure is adopted, not proposed as new; its value here is that it couples local wall superheat, evaporation–condensation processes and transient bubble dynamics, so that the effect of groove geometry on local phase-change intensity can be assessed rather than only overall heat-transfer trends.

Most importantly, this study aims to identify the best of the tested annular groove spacing-to-width (S/W) combinations from a combined analysis of vapor-generation behavior, vapor evacuation and thermal resistance. By revealing the competing roles of groove-induced vapor generation and vapor-retention limitation, the results provide mechanistic design guidance rather than empirical correlations; no universal optimum is claimed.

Collectively, this work advances heat pipe research from performance-based evaluation toward geometry-informed, CFD-driven, offering a transferable design framework for next-generation, high-performance thermosyphon and heat pipe systems.

Compared with Abdullahi [40], who provided temperature data for a smooth thermosyphon without inner-wall modification, the present study (i) uses their geometry and operating conditions as the validated base case, (ii) adds annular grooves and varies their spacing and width, (iii) moves from global wall-temperature and resistance measures to bubble-scale quantities from a transient VOF model with a temperature-driven phase-change UDF, and (iv) identifies a competing effect between vapor generation and vapor retention. Earlier work on grooved, corrugated or finned geometries [26,28,29,31,38,39] reports mainly global metrics and does not extract wall-attached vapor sites, vapor residence time or departure behavior as functions of annular groove spacing and width.

Rectangular annular grooves were chosen because they are defined by three parameters (width, depth, pitch), are easy to manufacture by turning or rolling, and are periodic in the longitudinal section, so they can be represented in a two-dimensional model. In a vertical wickless thermosyphon the condensate returns by gravity, so axial grooves, whose main role is capillary transport, add little to liquid return, whereas circumferential grooves enlarge the wetted area where boiling occurs. Spiral and axial grooves are inherently three-dimensional and other groove profiles are not considered here.

2. Methodology

2.1. System Description and Dimension

In the current research, a vertical two-dimensional heat pipe configuration was considered as the base model, as shown in Figure 1, like the setup previously investigated by Abdullahi [40]. Solar irradiance transmitted through the evacuated glass envelope is absorbed by the selective coating on the absorber and conducted to the evaporator section of the heat pipe. The working fluid evaporates, and the vapor rises through the adiabatic section to the condenser, which is inserted into the manifold of the horizontal storage tank. There the vapor releases its latent heat to the circulating water and condenses, and the condensate returns to the evaporator under gravity along the inner wall. The evacuated annulus suppresses convective and conductive losses, so that the dominant loss mechanism is radiation from the absorber surface.

Figure 2a shows the standard geometry, where the heat pipe is divided into two main sections, the evaporator and the condenser, featuring equal lengths and diameters, representing a symmetrical design. Figure 2b showcases the base case with a filling ratio of 65% (the ratio of liquid filling the evaporator), which adheres to the same specifications as Abdullahi's earlier research [40] on a heat pipe, serving as a reference for comparing and validating the current work simulations. Figure 2c,d introduces a modified design of the heat pipe, which is distinguished by the addition of annular grooves. These modifications are proposed to enhance the heat transfer efficiency and operational effectiveness of the heat pipe in practical applications. Table 2 summarizes.

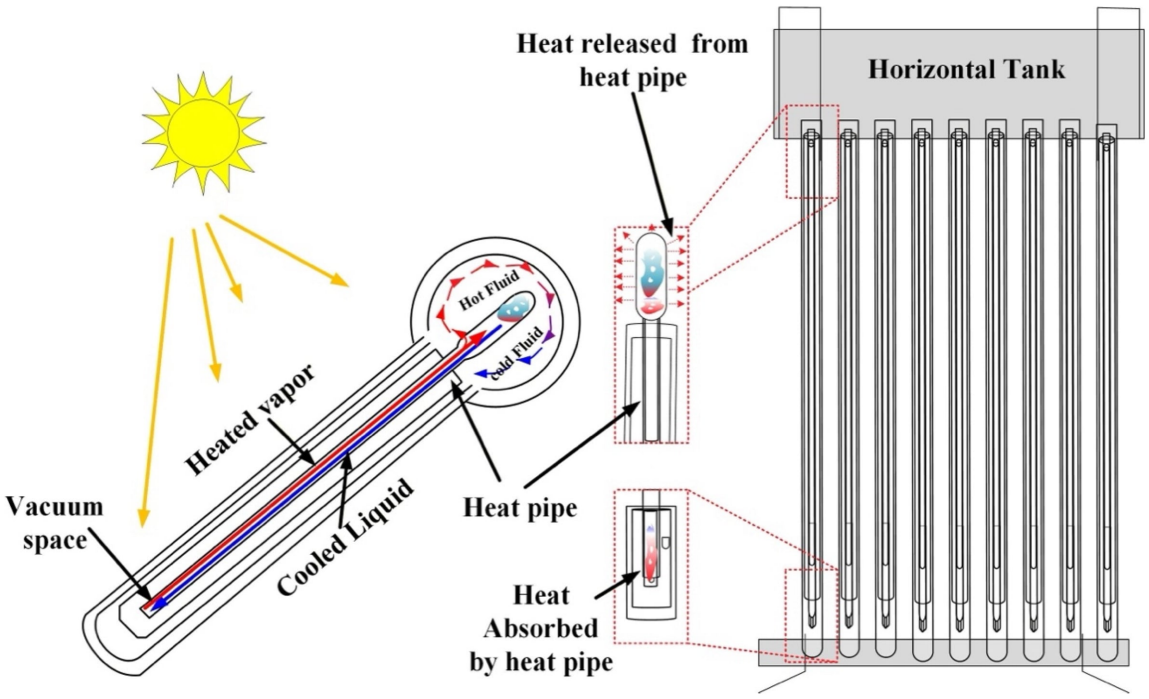


Figure 1. Schematic of heat-pipe-assisted evacuated solar tube collector. The cycle is as follows: (1) solar radiation is absorbed by the coated absorber; (2) the working fluid evaporates in the evaporator; (3) vapor rises through the adiabatic section; (4) vapor condenses in the manifold and releases heat to the tank water; (5) condensate returns by gravity along the wall.

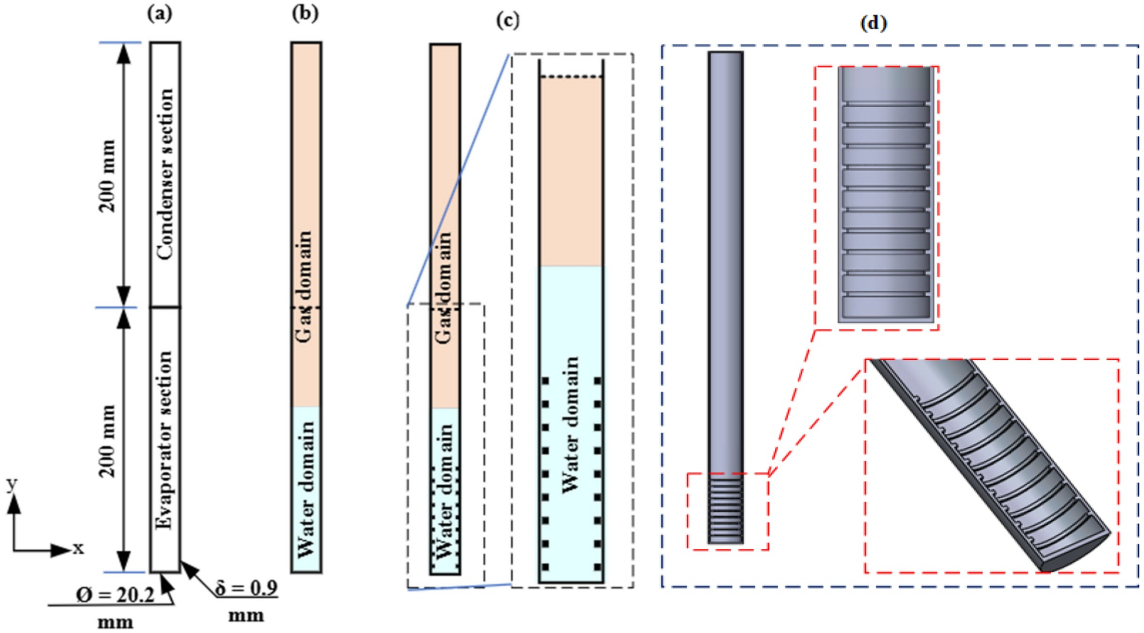


Figure 2. Heat pipe configurations: (**a**) Standard geometry with evaporator and condenser sections of equal length and diameter; (**b**) Base case identical to Abdullahi's heat pipe geometry; (**c**) Modified heat pipe design incorporating annular grooves. (**d**) Two-dimensional views of the new design. Groove dimensions: width W, depth d = 1.0 mm, pitch S (Table 3).

Table 2. Thermosyphon configuration and thermophysical properties.

Parameter	Value	Unit
Tube material	Copper	–
Outer diameter, D_o	22.0	mm
Inner diameter, D_i	20.2	mm
Wall thickness, t	0.9	mm
Total length, L	400	mm
Evaporator length, Le	200	mm
Condenser length, Lc	200	mm
Working fluid	Water	–
Filling ratio	65	%
Orientation	Vertical	–
Heat input, Q	81 and 101	W
Evaporator heat flux (outer wall)	5860 and 7307	W m^{-2}
Condenser convective coefficient, hc	706	W m^{-2} K^{-1}
Copper: density/specific heat/conductivity	8978/381/387.6	kg m^{-3}/J kg^{-1} K^{-1}/W m^{-1} K^{-1}
Liquid water at 373.15 K: ρ/cp/k/μ	958.4/4217/0.679/2.82 × 10^{-4}	kg m^{-3}/J kg^{-1} K^{-1}/W m^{-1} K^{-1}/Pa s
Water vapour at 373.15 K: ρ/cp/k/μ	0.5978/2029/0.0248/1.202 × 10^{-5}	kg m^{-3}/J kg^{-1} K^{-1}/W m^{-1} K^{-1}/Pa s
Surface tension at 373.15 K, σ	0.0589	N m^{-1}
Latent heat used in the UDF, hfg	2455	kJ kg^{-1}

Table 3. Groove Geometry used in the CFD Domain.

Groove depth	1 mm
Groove width	1 mm
Groove width(variation)	0.5, 1.0, 1.5 mm
Groove spacing (variation)	2.5, 5.0, 10 mm
Number of grooves	10
Groove shape	Rectangular annular
Location: Evaporator section	Lower 200 mm

Copper–water was selected because it is the standard working pair for wickless thermosyphons in the 30–200 °C range: water has a high latent heat (2455 kJ kg^{-1} at 373 K) and high surface tension, and copper has high conductivity and is chemically compatible with water without generating non-condensable gas [10]. It is also the pair used in evacuated-tube collector heat pipes. The heat inputs of 81 W and 101 W are the two power levels of the experiment of Abdullahi [40], so the same conditions are used for validation and for the parametric study; they correspond to evaporator outer-wall heat fluxes of 5.86 and 7.31 kW m^{-2}, of the order of the solar power intercepted by one evacuated tube at about 1000 W m^{-2} (a typical 58 mm × 1800 mm evacuated tube intercepts about 104 W at 1000 W m^{-2} on its projected area). The heat flux is the heat input divided by the outer evaporator wall area, $\pi D_o L_e = 0.0138$ m^2. The condenser coefficient $h_c = 706$ W m^{-2} K^{-1} is taken from the same experiment and is used for the validation and all parametric cases.

The filling ratio of 65% is the reference condition of the validation experiment [40] and lies within the range of 50–70% usually recommended for water-filled thermosyphons, which keeps a continuous liquid pool in the evaporator and avoids both dry-out and flooding of the condenser [10,41]. At 65% the pool height is 130 mm, which submerges the whole grooved region for every simulated spacing.

The tube (22 mm outer diameter, 0.9 mm wall, 400 mm length) is a standard copper tube size (22 × 0.9 mm is a listed size in EN 1057) and the size of the experimental thermosyphon used for validation; evacuated-tube collector heat pipes are longer, so the

model represents a section of such a pipe. The rectangular annular grooves (0.5–1.5 mm wide, 1.0 mm deep, 2.5–10 mm pitch) are within the range achievable by internal turning or rolling. Because the groove depth (1.0 mm) is larger than the wall thickness (0.9 mm), the grooves are taken as recesses cut into a locally thicker wall or formed in an inserted grooved ring. Each groove is a rectangular recess of width W, depth d and pitch S (Table 3, Figure 2).

2.2. System Modelling

This section covers the 2D CFD simulation of the heat pipe and the methodology used. The present study employed a two-dimensional planar model with boundary conditions that well captured detailed quantitative insights into bubble-scale dynamics and groove-induced performance changes. The Volume of Fluid (VoF) multiphase model was employed to simulate evaporation and condensation in the heat pipe. The VoF model was chosen owing to its ability to precisely capture the interface between the gas and liquid phases, which is critical for simulating phase-change phenomena. This model assigns a volume fraction to each phase within a computational cell, enabling precise depiction of gas–liquid interface dynamics. The VoF method is a surface-tracking technique applied to a fixed Eulerian mesh, in which a single set of momentum and energy equations is solved for the phase mixture, and the interface is located by transporting the volume fraction of each phase. Within this framework, the phases share the velocity, pressure, and temperature fields, and each computational cell contains either a single phase or a mixture of both.

Two main approaches are commonly used to model multiphase flows: the Euler–Lagrange and Euler–Euler methods. In the Euler–Lagrange approach, the continuous fluid phase is treated as a continuum. In contrast, the dispersed phase (e.g., bubbles) is modeled as a separate, discrete phase, with volume fractions not exceeding 10% [42]. Since the current application involves a second phase with volume fractions exceeding 10%, the Euler–Euler approach was chosen in this current study. This approach uses the concept of phasic volume fractions, ensuring that no phase can occupy the volume of another. These volume fractions are considered continuous functions of both space and time.

The accuracy of the VoF model in tracking the interface stems from its approach of solving a single set of momentum equations while monitoring the volume fraction of each fluid across the entire domain. This method ensures a sharp, well-defined interface between the phases, which is essential for accurately capturing the evaporation and condensation processes. The VoF model can also handle large density differences between phases, making it suitable for simulating complex behaviors in a thermosyphon heat pipe [43]. Furthermore, using a fixed mesh for surface tracking, the VoF technique is used to simulate two immiscible fluids with a well-defined interface separating the phases. In this model, a single set of Navier–Stokes equations is solved throughout the computational domain, and the motion of each phase is tracked using its respective volume fractions. It is assumed that each computational cell contains either a single phase or a mixture of both phases. Letting αL denote the volume fraction of liquid and αV that of vapor, for a two-phase system, the volume fractions satisfy $\alpha L + \alpha V = 1$ in every computational cell. Three states are therefore distinguished:

Basis for model selection. The objective is the shape, attachment and departure of individual vapor bubbles around the groove geometry. VOF tracks the interface on a fixed mesh with a sharp front and handles the large density ratio (about 1600). Mixture and Eulerian–Eulerian models average the interface, and the Eulerian wall-boiling model replaces bubble behavior with empirical correlations for site density, departure diameter and frequency, which are the quantities examined here [44]. A

temperature-driven Lee-type closure was chosen because it has been used successfully with VOF for thermosyphons [16,19,37], needs no cavity-size or contact-angle input, and conserves mass and energy through the volume-fraction and energy equations. ANSYS Fluent 2025 R2 was used because it provides a sharp-interface VOF implementation with geometric reconstruction, the CSF surface-tension model, conjugate heat transfer through coupled walls, and user-defined functions for the phase-change sources; it has also been used in most of the thermosyphon CFD studies compared here [14,16,37]. The approach is not tied to one code.

- $\alpha L = 1$ ($\alpha V = 0$): the cell contains only liquid;
- $\alpha L = 0$ ($\alpha V = 1$): the cell contains only vapor;
- $0 < \alpha_L, \alpha_v < 1, \ni \alpha_L + \alpha V = 1$: the cell contains the liquid–vapor interface.

The following assumptions were adopted for the current model:

- Two-dimensional planar longitudinal domain.
- Laminar flow in both phases (vapor Reynolds number about 2×10^2 at 101 W, from a vapor mass flow of 4.1×10^{-5} kg s^{-1} in the 20.2 mm bore; unsteady flow driven by bubble growth and departure is resolved, but small-scale turbulence in the bubbly or churn regime is not modelled).
- Newtonian, incompressible phases; constant vapor properties, viscosities, conductivities and specific heats at 373.15 K (liquid density and surface tension depend on temperature, Equations (5) and (7)) (Table 2).
- Homogeneous VoF: shared velocity, pressure, and temperature fields.
- Saturation temperature fixed at 373.15 K.
- Constant latent heat of vaporization, hfg = 2455 kJ kg^{-1}.
- Lee-type phase change with relaxation coefficient $\beta = 0.1$ s^{-1}.
- No cavity-activation (nucleation-site) criterion.
- Temperature-dependent surface tension $\sigma(T)$, Equation (5) (0.0589 N m^{-1} at 373.15 K); CSF model; no wall-adhesion model.
- Viscous dissipation and radiative exchange are neglected.
- Perfect thermal contact at the solid–fluid interface (coupled wall).
- Adiabatic top and bottom end caps.
- Constant convective coefficient at the condenser outer wall.
- Copper properties are constant and isotropic; no oxidation or fouling.
- Grooves are ideal rectangular recesses.
- No wick; gravity-assisted condensate return, vertical orientation.

The volume fractions of all phases sum to 1 in the third condition. The main drawbacks in simulating phase change materials during evaporation and condensation processes with the VoF evaporation and condensation model in FLUENT 2025 R2. Hence, a user-defined function (UDF) was implemented to overcome this limitation and extend FLUENT's capabilities. This UDF is essential for calculating the mass and heat transfer between the liquid and vapor phases during phase change. These calculations are derived from the source terms present in the governing equations, particularly the continuity and energy equations. The source terms were used to compute the mass and energy transfer as proposed by [37]. This study employed the mass source term (Sm) in the volume fraction equation and the energy source term (Se) in the energy equation. These source terms are detailed in the UDF to ensure accurate modeling of mass and heat exchanges by dynamically adjusting them based on local thermodynamic conditions. This approach enables precise simulation of evaporation and condensation, thereby enhancing the CFD model's accuracy in predicting the thermosyphon heat pipe's performance. In the present model, water vapor is designated as the primary phase

and liquid water as the secondary phase. To simulate mass and heat transfer during evaporation and condensation, a boiling point of 373 K is employed, with the latent heat set to 2455 kJ/kg via the UDF code. Initially, the liquid pool in the evaporator is heated, and once its temperature reaches the saturation temperature of 373 K, the phase change begins as evaporation. The generated saturated vapor ascends to the condenser, where it condenses on the cold walls, forming a thin liquid film.

2.2.1. Numerical Implementation and Reproducibility Details

To enable full replicability of the CFD model and UDF-based phase change framework, the numerical implementation, groove geometry parameters, solver configuration, and time-step sensitivity are summarized in this subsection. The PREssure STaggering Option (PRESTO!) scheme was selected for pressure interpolation. Standard interpolation schemes assume a smooth pressure variation between cell centers, an assumption that fails across a liquid–vapour interface, where the density ratio exceeds 1600, and the body force and surface-tension terms produce a steep, discontinuous pressure gradient. PRESTO! reproduces the staggered-grid treatment in the unstructured solver by computing face pressures from a discrete continuity balance on a staggered control volume, and is the recommended scheme for VOF simulations dominated by buoyancy and surface tension.

- UDF-Based Phase Change Model

Evaporation and condensation were modeled using a temperature-dependent user-defined function (UDF), which introduces mass and energy source terms when local cell temperature deviates from the saturation temperature of water at 373 K. The UDF framework ensures consistent coupling between phase change, energy transfer, and interface motion. The conceptual pseudocode governing the phase-change logic is provided below:

```
        if (Tcell > Tsat) then          // evaporation
    compute mass source Sm ∝ (Tcell − Tsat)
    compute energy source Se = Sm × hfg
else if (Tcell < Tsat) then    // condensation
    compute condensation mass sink
    compute corresponding energy sink
end if
```

This algorithm ensures thermodynamically consistent coupling between temperature deviations and mass/energy transfer during phase change.

The formulation of the Lee-type closure and its assumptions are given with the governing equations in Section 2.3 (Equations (13)–(15)). The relaxation coefficient $\beta = 0.1\ s^{-1}$ is the value used in the source-term formulations of Alammar et al. [16] and Fadhl et al. [37], which follow De Schepper et al. [45]; it was not tuned to the experimental data.

- Groove Geometry Used in the CFD Domain

The evaporator section incorporates regularly spaced annular grooves. All geometric parameters necessary for reproducing the computational domain are summarized in Table 3.

The groove depth (1.0 mm) exceeds the wall thickness (0.9 mm) in Table 2, so the grooves are treated as recesses as described in Section 2.1. With ten grooves in the lower evaporator (Table 3), the grooved length is about 100, 50 and 25 mm for S = 10, 5 and 2.5 mm, respectively, all inside the 130 mm liquid pool at 65% filling.

- Time-Step Sensitivity Analysis

A time-step independence assessment was conducted using $\Delta t = 5 \times 10^{-4}$ s, 1×10^{-4} s, and 5×10^{-5} s. For each configuration, vapor volume fraction, wall temperature, and interface reconstruction stability were monitored. The Key findings were variation in

average vapor fraction was <1.8%, the maximum wall temperature deviation was <0.9 K and Interface stability improved at $\Delta t = 1 \times 10^{-4}$ s. Thus, a time step of 1×10^{-4} s was adopted.

- Numerical Solver Settings

Simulations were performed using the pressure-based transient solver with the following settings as shown in Table 4.

Table 4. Numerical Solver Settings.

Pressure–velocity coupling	Semi-Implicit Method For Pressure-Linked Equations (SIMPLE)
Pressure interpolation	PRESTO!
Momentum:	First-order upwind
Energy:	First-order upwind
Volume fraction	Geo-Reconstruct
Gradient reconstruction	Least-squares cell-based
Transient formulation	First-order implicit

- Convergence and Computational Requirements

Each step was iterated until residuals were satisfied with continuity, momentum was set to less than 10^{-4}, energy and volume fraction were set to less than 10^{-6}.

2.2.2. Statistical Considerations

This study is based on deterministic computational fluid dynamics (CFD) simulations, and therefore no stochastic sampling, randomization, or experimental replications are involved. As a result, statistical tests such as confidence intervals, hypothesis testing, *p*-values, or effect size analysis are not applicable. All results are directly obtained from numerical solutions of the governing equations, and reproducibility is ensured through the mesh-independence study, time-step sensitivity analysis, solver settings, and UDF implementation details provided in the methodology. Deterministic CFD has no sampling error, but it has discretization, iteration and model-form uncertainty, which are discussed in Sections 2.5 and 3.2.

2.3. Governing Equations of Flow and Heat Transfer

- Navier–Stokes equations for VoF model

The behaviour of the working fluid in a thermosyphon is described by the governing equations of mass continuity, momentum, and energy. These fundamental equations are essential for understanding the system's fluid dynamics and heat transfer processes. The subsections provide a detailed explanation of these equations and their application in the context of a thermosyphon. The equations follow the VOF method of Hirt and Nichols [46], the continuum surface force model of Brackbill et al. [47], the mass-transfer closure of Lee [48] in the form used by Fadhl et al. [37] and Alammar et al. [16] (source terms after De Schepper et al. [45]), and the formulation in the Fluent theory guide [43]; see also Faghri [10]. Vectors and tensors are written in bold and scalars in italics.

- Continuity equation

The continuity equation is obtained by applying the basic principle of mass conservation to the fluid. This equation ensures that the mass of the fluid remains constant as it flows through the thermosyphon. The mathematical expression of the continuity equation is given by:

$$\nabla\cdot\left(\rho\vec{u}\right) = -\frac{\partial\rho}{\partial t} \quad (1)$$

where ρ is the density, u is the velocity, and t is the time.

By solving Equation (1) for the volume fraction of one of the phases, the interface between the phases can be effectively tracked. Accordingly, the continuity equation for the secondary phase (L) in the VoF model can be written as:

$$\nabla\cdot\left(\alpha_L\rho_L\vec{u}\right) = -\frac{\partial}{\partial t}(\alpha_L\rho_L) + S_m \quad (2)$$

The continuity equation shown above is commonly known as the volume fraction equation. where ρ is the density (kg m^{-3}), u is the velocity vector (m s^{-1}), S_m is the volumetric mass source (kg m^{-3} s^{-1}), and Se is the volumetric energy source (W m^{-3}).

It is not solved for the primary phase directly; rather, the volume fraction of the primary phase is obtained using the following constraint:

$$\sum_{L=1}^{n}\alpha_L = 1 \quad (3)$$

When a cell contains both the primary and secondary phases, it represents a mixture of the two. In this case, the mixture density is calculated as a volume-fraction-weighted average, expressed by the following formula:

$$\rho = \alpha_L\rho_L + (1-\alpha_L)\rho_V \quad (4)$$

- Momentum equation

The fluid is subjected to various forces, including gravity, pressure, friction, and surface tension. Gravitational acceleration (g) is applied in the negative y-direction. Surface tension effects are modeled using the Continuum Surface Force (CSF) approach developed by Brackbill et al. [47] is incorporated into the momentum equation to account for the influence of surface tension at the interface between the two phases.

$$\sigma_{LV} = 0.09805856 - 1.845\times10^{-5}T - 2.3\times10^{-7}T^2 \quad (5)$$

where σ_{LV} represents the surface tension coefficient, and C denotes the surface curvature. This coefficient was used to calculate the F_{CSF} using the following equation:

$$F_{\mathrm{CSF}} = 2\sigma_{LV}\frac{\alpha_L\rho_L C_V\nabla\alpha_V + \alpha_V\rho_V C_L\nabla\alpha_L}{\rho_L+\rho_V} \quad (6)$$

The density of the liquid water phase was considered temperature dependent. The following polynomial equation was used to express this relationship:

$$\rho_L = 859.0083 + 1.252209T - 0.0026429T^2 \quad (7)$$

In Equations (5) and (7), σ_{LV} is in N m^{-1}, ρ_L in kg m^{-3} and T in K, used over the simulated temperature range (about 290–385 K). At 373.15 K they give 0.0591 N m^{-1} and 958.3 kg m^{-3}, consistent with Table 2 (0.0589 N m^{-1} and 958.4 kg m^{-3}).

Now, the momentum equation is as follows:

$$\frac{\partial}{\partial t}(\rho\vec{u}) + \nabla\cdot(\rho\vec{u}\vec{u}) = \rho\vec{g} - \nabla p + \nabla\cdot\left[\mu\left(\nabla\vec{u} + \nabla\vec{u}^T\right) - \frac{2}{3}\mu\nabla\cdot uI\right] + F_{\mathrm{CSF}}. \quad (8)$$

where p represents the pressure, and I is the unit tensor. The above equation is influenced by the α of all phases, as it incorporates the physical properties of density and viscosity. Consequently, the dynamic viscosity μ is given by:

$$\mu = \alpha_L \mu_L + (1 - \alpha_L)\mu_V \quad (9)$$

A single momentum equation is solved across the entire computational domain. The resulting velocity field is then shared among all phases, ensuring a consistent representation of fluid flow. This allows for the accurate representation of interactions between the different phases, accounting for the influence of each phase on the overall velocity distribution.

- Energy equation

The energy equation, modified to include the energy source term, is expressed as follows:

$$\frac{\partial(\rho E)}{\partial t} + \nabla \cdot [u(\rho E + p)] = \nabla \cdot (k \nabla T) + S_E \quad (10)$$

where E and K denote the internal energy and thermal conductivity, respectively. These terms were calculated from the following equations, specifically for the mixture.

$$k = \alpha_l k_l + \alpha_v k_v \quad (11)$$

$$E = \frac{\alpha_l \rho_l C p_l + \alpha_v \rho_v C p_v}{\alpha_l \rho_l + \alpha_v \rho_v} (T - T_{sat}) \quad (12)$$

where k_L and k_V are the thermal conductivities of the liquid and gas phases, respectively, and Cp_l and Cp_V are the specific heats of the liquid and vapor phases, respectively.

Phase-change source terms (Lee-type closure). Mass is transferred from liquid to vapor where the cell temperature exceeds T_{sat} and from vapor to liquid where it is below T_{sat}. The assumptions are saturation at a constant $T_{sat} = 373.15$ K, constant $h_{fg} = 2455$ kJ kg^{-1}, and local thermal equilibrium in each cell. The mass-transfer rates (kg m^{-3} s^{-1}) are:

$$\dot{m}_{lv} = \beta \alpha_L \rho_L \frac{T - T_{sat}}{T_{sat}} \ (T > T_{sat}) \quad (13)$$

$$\dot{m}_{vl} = \beta \alpha_V \rho_V \frac{T_{sat} - T}{T_{sat}} \ (T < T_{sat}) \quad (14)$$

$$S_m = \dot{m}_{vl} - \dot{m}_{lv}, \ S_E = -h_{fg}(\dot{m}_{lv} - \dot{m}_{vl}) \quad (15)$$

where S_m acts on the liquid volume-fraction equation (Equation (2)) and S_E in the energy equation (Equation (10)). The relaxation coefficient β is a numerical time constant (s^{-1}); a smaller value lets the interface depart from T_{sat}, whereas a larger value forces it toward T_{sat} but can destabilise the solution. The closure has no nucleation-site activation criterion and no contact-angle model.

2.4. Boundary Conditions, Initial Conditions, and Patching

Boundary conditions were established in the current model, as shown in Figure 3. A constant heat flux boundary was defined for the heater wall, while a convective boundary condition ($h_c = 706$ W m^{-2} K^{-1}, ambient temperature $T_\infty \approx 290$ K was specified for the condenser outer wall. The equivalent heat-flux values (approximately 5.86 kW/m^2 for 81 W and 7.307 kW/m^2 for 101 W, based on the evaporator wall area of 0.0138 m^2) The boundary conditions and initial settings for the heat pipe simulation were carefully defined to model the thermal and fluid dynamics accurately. The top and bottom walls of the heat pipe were specified as adiabatic, meaning they do not allow heat transfer through them, ensuring thermal insulation. The interfaces between the solid and fluid phases were configured as coupled walls, allowing conjugate heat transfer between the solid and fluid domains.

To initialize the simulation, 65% of the evaporator region was patched with the liquid phase, ensuring sufficient liquid for the phase change process. The temperature within the evaporator was set slightly above the saturation temperature, at 373.3 K, to promote

evaporation. Conversely, the condenser section was patched with a lower temperature of 323.3 K to facilitate vapour condensation. In addition, the liquid phase was also set to zero in the upper 35% of the evaporator section and the whole condenser section. This setup ensured that these regions were initially filled with vapour, creating a realistic starting condition for the simulation.

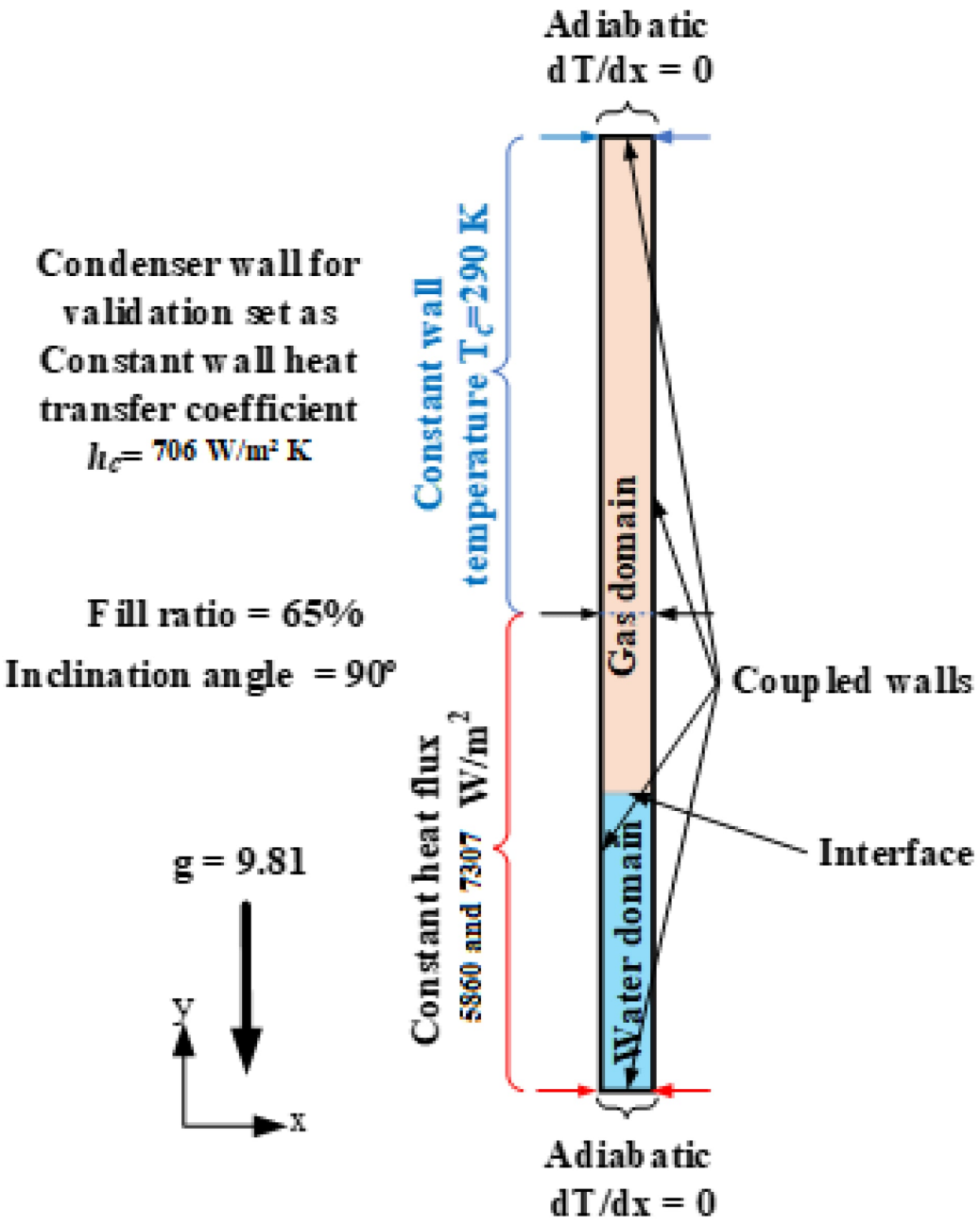


Figure 3. Schematic representation of the boundary conditions applied in the CFD model, illustrating the heat flux boundary at the heater wall and the convective boundary (h_c = 706 W m^{-2} K^{-1}) at the condenser wall.

The boundary and initial conditions are summarised in Table 5. The heat-flux values are based on the outer evaporator wall area $\pi D_o L_e$ = 0.0138 m^2.

Table 5. Summary of boundary and initial conditions.

Boundary/Initial Condition	Specification
Evaporator outer wall (heated)	Constant heat flux: 5.86 kW m^{-2} (81 W); 7.31 kW m^{-2} (101 W)
Condenser outer wall	Convection: hc = 706 W m^{-2} K^{-1}, T∞ ≈ 290 K (Section 2.4)
Top and bottom end caps	Adiabatic
Solid–fluid interfaces	Coupled walls (conjugate heat transfer)
Gravity	9.81 m s^{-2}, in the −y direction
Operating pressure	101.325 kPa (consistent with T_{sat} = 373.15 K)
Initial liquid fill	65% of the evaporator patched with liquid; vapor elsewhere
Initial temperature	Evaporator 373.3 K; condenser region 323.3 K

2.5. Geometry and Mesh

The heat pipe's geometries, as shown in the previous section, were constructed using the Ansys design modeler. In all cases, the heat pipe configuration consists of a copper tube with a thickness of 0.9 mm, a total height of 400 mm, and outer and inner diameters of 22 mm and 20.2 mm, respectively. The thermosyphon is divided into two equal sections (evaporator and condenser), each 200 mm in height, as depicted in Figure 2. These dimensions are the same as those used in prior experimental and mathematical work, and Alammar et al.'s work was used to validate the CFD simulation. Then, Ansys Mesh was used to create a structured mesh to discretize the computational domain, ensuring high accuracy in the regions with higher gradients. A structured quadrilateral grid was generated with local refinement in the groove region and near the liquid–vapor interface. Three grid densities (28k, 52k and 96k cells) were used for the mesh-independence study (Section 2.5). The Courant number was maintained below 0.25 throughout. The fluid domain comprised about 25,000 cells and the solid domain about 10,000 cells.

Mesh independence was examined with three structured grids of 28k, 52k and 96k cells. The predicted vapor volume fraction differed by less than 2.3% between the medium and fine grids, so the results are independent of the grid within this tolerance. The time step was examined at $\Delta t = 5 \times 10^{-4}$, 1×10^{-4} and 5×10^{-5} s: the average vapor fraction varied by less than 1.8% and the maximum wall temperature by less than 0.9 K, and $\Delta t = 1 \times 10^{-4}$ s gave the most stable interface and was adopted. The smooth and grooved pipes are computed on the same mesh and time step, so their relative differences are consistent across cases.

2.6. Solution Procedure

A transient simulation was performed with a time step of 1×10^{-4} s to accurately capture the dynamic behavior of the two-phase flow. This step was chosen based on the Courant number, which links the time step to the time required for fluid to pass through a computational cell. With this selection, the Courant number remains at or below 0.25, as required by the explicit Geo-Reconstruct scheme throughout the simulation. Steady-state conditions are achieved after approximately 60 s. The Courant–Friedrichs–Lewy (CFL) condition was applied to ensure numerical stability in solving partial differential equations, especially when using explicit time-stepping methods. The CFL condition guarantees that the numerical domain of dependence encompasses the physical domain of dependence and is mathematically expressed as:

$$Co = \frac{|u|\Delta t}{\Delta x} \leq 0.25\Delta \quad (16)$$

Here, u represents the characteristic flow velocity, Δt is the time step size, and Δx is the spatial grid size. The model uses the SIMPLE algorithm for pressure-velocity coupling and employs a first-order upwind scheme for momentum and energy calculations. Additionally, the Geo-Reconstruct method and PRESTO discretization are applied for volume fraction and pressure interpolation, respectively. Numerical convergence in this study is achieved when the scaled residuals for mass and velocity components drop below 10^{-4}.

In Equation (16), |u| is the magnitude of the local mixture velocity in a cell, Δx is the local cell size in the flow direction, and Co is the largest cell value over the domain, evaluated by the solver at every time step; the time step was chosen to keep Co below the limit of 0.25 required by the explicit Geo-Reconstruct scheme.

2.7. Post-Processing Metrics and Verification Workflow

Bubble and site identification. A vapor structure is a connected region of cells with $\alpha_V \geq 0.5$. It is counted as a wall-attached vapor site while it shares a cell face with the inner wall of the evaporator, and as detached when it no longer does. Residence time is the interval between first attachment and detachment, the departure interval is the time between successive detachments at the same site, the departure frequency is its reciprocal, and the departure diameter is the equivalent-area diameter of the structure at detachment. The counts reported in Section 4 were taken from the saved vapor-fraction fields at the output times shown in Figures 7, 8 and 11, with identical thresholds for all cases. Percentage changes are $(X_{groove} - X_{ref})/X_{ref}$. Because the Lee-type closure has no sub-grid nucleation model, these quantities describe grid-resolved vapor structures and are comparative, not physical nucleation-site densities.

Verification and validation workflow. The model is a physics-based CFD model; no training or test data set is involved. The workflow has four steps: (1) governing equations and closure (VOF with a temperature-driven Lee-type UDF, $\beta = 0.1\ s^{-1}$ from the literature [37], not tuned); (2) solution verification (mesh and time-step tests, Section 2.5; residuals); (3) validation of the smooth pipe against experiment (Section 3.1); (4) application to the parametric cases (Section 4), with the grooved cases assessed as described in Section 3.3.

3. Validation

3.1. Comparison with Experiment

The current study was validated against the findings of Abdullahi [40] and Alammar et al. [16] under identical conditions for the heat pipe. Specifically, a power of 101 W was applied at the heater section, while a convective heat transfer coefficient of 706 W/m^2 K. was employed at the condenser section. A filling ratio of 65% was used for this validation. The average variation between the experimental data and the model results amounted to approximately 4.15% for both the heater and condenser wall temperatures (arithmetic mean of the relative deviations at the five measurement points, on the absolute temperature scale; maximum about 5.7% at y = 0.35 m, Table 6), as illustrated in Figure 4.

Table 6. Point-by-point comparison with the experiment of Abdullahi [40] (101 W) and with the CFD of Alammar et al. [16]. Values are read from Figure 4 (±1–2 K); the mean of the present deviations (3.9%) is therefore close to the 4.15% quoted in the text.

y (m)	Exp. (K)	Present (K)	Dev. (%)	Alammar et al. [16] (K)	Dev. (%)
0.02	392.5	374.5	4.6	386	1.7
0.07	389.5	374.7	3.8	393	0.9
0.12	386.5	374.8	3.0	389	0.6
0.25	305	297	2.6	303	0.7
0.35	308.5	291	5.7	295.5	4.2
Mean/max			3.9/5.7		1.6/4.2

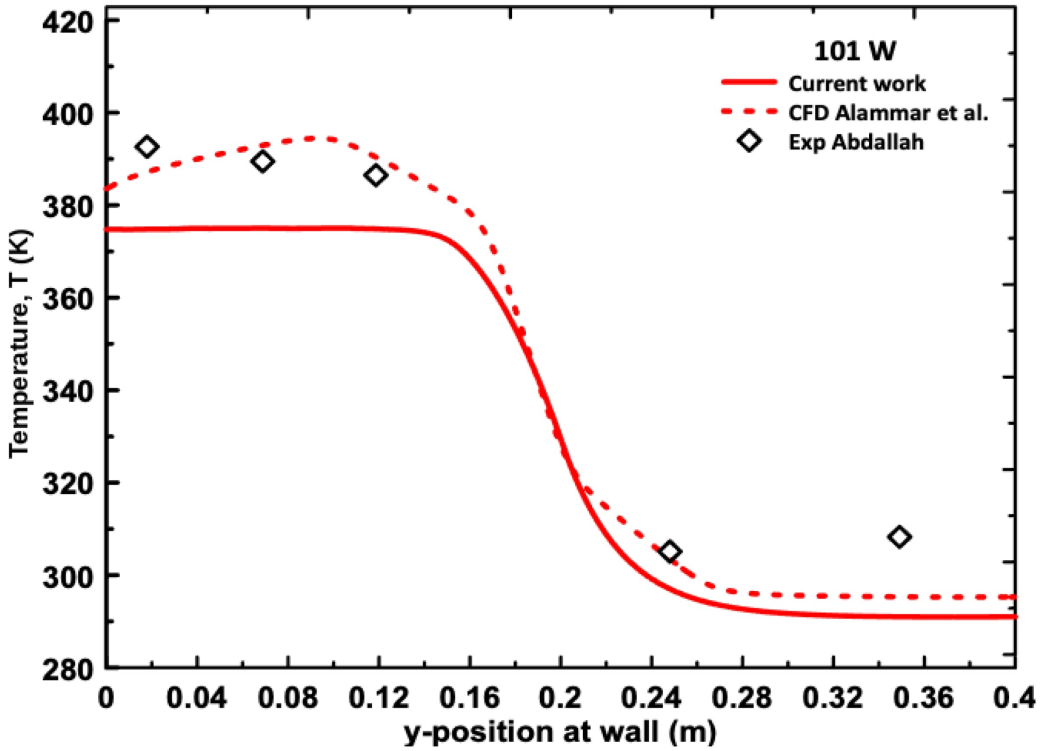


Figure 4. Comparison between CFD work of [16] and experimental data of [40] and the current study for temperature variation along heat pipe wall y-position.

The validation case is the thermosyphon of Abdullahi [40]: copper tube, D_o = 22 mm, D_i = 20.2 mm, L = 400 mm with 200 mm evaporator and 200 mm condenser; water at 65% filling ratio; vertical; heat input 101 W applied as 7.31 kW m^{-2} on the evaporator outer wall; condenser cooled by convection with h_c = 706 W m^{-2} K^{-1} and T_∞ as in Section 2.4; adiabatic end caps. The experimental wall temperatures were measured at five axial positions (y = 0.02, 0.07, 0.12, 0.25 and 0.35 m). The model settings are those of Tables 4 and 5 and Section 2.5.

The present model reproduces the axial temperature profile, with the largest deviation (about 5.7%) at the condenser end (y = 0.35 m), where the predicted wall temperature of about 291 K is below the measured 308 K. In the evaporator the present model underpredicts the wall temperature by about 12–18 K (3–4.6%), whereas the model of Alammar et al. [16] is closer to the data (within about 7 K). Possible reasons for the difference between the two models include the domain treatment (planar vs. axisymmetric), the phase-change

coefficients and the heat-loss treatment. All parameters of the present model are literature values and were not tuned, and the same settings are used for the grooved cases, so the grooved-versus-smooth comparison is made with identical settings.

3.2. Numerical and Experimental Uncertainty

Numerical uncertainty was controlled through the mesh and time-step tests (Section 2.5) and a residual criterion of 10^{-4}. All model parameters are literature values and were not tuned to the experiment, and the deviations of 2.6–5.7% from the measured wall temperatures were obtained on this basis.

3.3. Support for the Grooved Cases

Experimental data for annular-grooved wickless thermosyphons at these operating conditions are not available in the literature reviewed, so the grooved cases are assessed in two ways. (i) The grooved cases use the same mesh strategy, time step and phase-change settings as the validated smooth case, so the grooves change the geometry only. (ii) The trends (lower local wall temperature with grooves at higher heat input, effect of groove spacing) are consistent in direction with grooved and corrugated thermosyphon studies [28,29,38]. The grooved-pipe results are therefore presented as comparative, and the bubble-scale numbers are comparative between cases.

4. Result and Discussion

4.1. Phase Distribution and Vapor Generation Characteristics

Numerical simulations were conducted to analyze the two-phase behavior within heat pipes under various thermal loads and geometrical configurations. Figure 5 depicts the vapor–liquid phase distribution contours at key axial positions for four different cases: (a) 81 W in a smooth pipe, (b) 81 W in a grooved pipe, (c) 101 W in a smooth pipe, and (d) 101 W in a grooved pipe. In all contour plots, blue regions correspond to the liquid phase, while red regions denote the vapor phase. At the onset of heating, the working fluid reaches its saturation temperature, triggering nucleation near the heated wall where the local wall temperature exceeds the saturation point. Initially, discrete vapor bubbles form within the continuous liquid matrix and adhere to the inner wall surface. As heating progresses, these bubbles grow due to continued energy input and eventually detach, driven by buoyancy and hydrodynamic forces from the surrounding liquid. This detachment marks the onset of bubbly flow, with vapor bubbles rising vertically and merging into larger structures as they ascend, indicating the transition toward slug or churn flow regimes.

A comparison between the smooth and grooved pipes under identical heat loads reveals critical insights. In the smooth pipe configurations (Figure 5a,c), vapor first appears as isolated structures in the superheated liquid layer next to the heated wall, with fewer wall-attached vapor sites (Figure 5) and later bubble formation. In contrast, the grooved pipes (Figure 5b,d) demonstrate enhanced nucleation predominantly along the wall surface. In the model, the grooves enlarge the wetted area and act as geometric pockets (no cavity-activation criterion is used), intensifying localized superheating and providing numerous preferential sites for vapor formation. This spatial shift in nucleation behavior leads to more uniform, denser vapor production along the evaporator section. At 81 W heat input, vapor formation is moderate in both geometries, but the grooved configuration exhibits a denser distribution of vapor bubbles near the wall due to the augmented surface area and thermal agitation. At an elevated heat input of 101 W, nucleation intensifies in both configurations; however, the grooved pipe exhibits a more homogeneous vapor layer enveloping the heated surface, indicating more intense, partly wall-covering vapor generation along the grooves (a continuous vapor film was not observed; see Section 4.5). This behavior underscores

the groove-induced enhancement in boiling heat transfer. A quantitative evaluation of the average vapor fraction further substantiates the thermal performance benefits of the grooved geometry. Over the simulated period the average evaporator vapor fraction of the grooved pipe at 101 W was about 12% higher than that of the smooth pipe (Figure 9). This increase in vapor-generation efficiency directly correlates with improved wall heat-flux removal, highlighting the superiority of grooved surfaces in managing high thermal loads. Additionally, faster vapor transport toward the condenser section is evident in the grooved pipes. The enhanced bubble detachment and vertical coalescence, associated with the larger wetted area, the higher local superheat and the buoyancy-driven liquid motion resolved by the model, contribute to lower local wall temperature and faster phase transport (the effect on overall thermal resistance is discussed in Section 4.6). These findings align with the recent literature emphasizing the role of surface modifications in enhancing nucleate boiling performance and regulating two-phase flow.

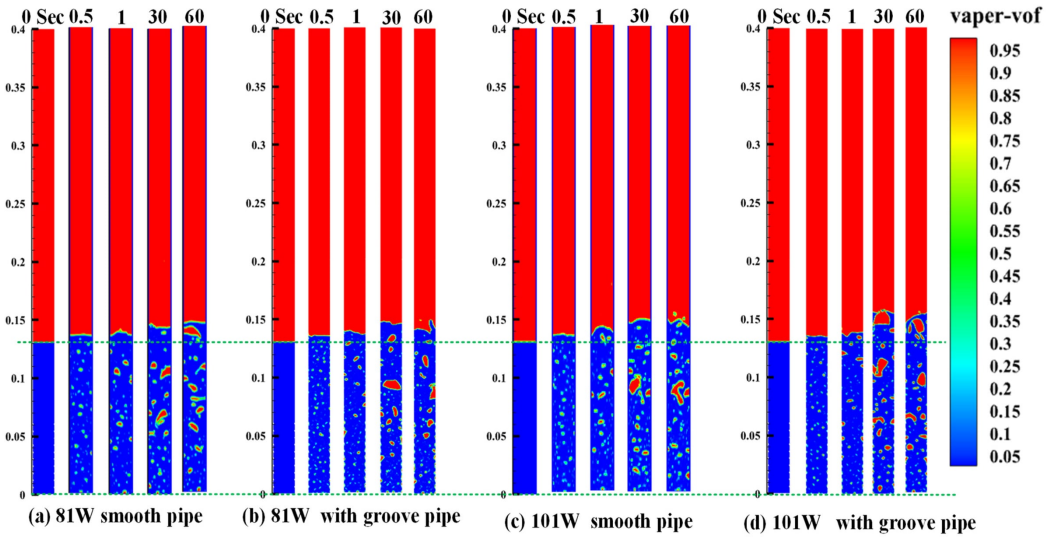


Figure 5. Vapor volume fraction contours for various computational times with heat inputs of 81 W and 101 W, illustrating the differences between smooth and grooved heat pipes.

4.2. Temperature Distribution Analysis: Effect of Surface Geometry on Thermal Response

Figure 6 illustrates the transient temperature contours of smooth and grooved heat pipe configurations at two distinct heat inputs, 81 W and 101 W, over selected computational time steps: (a) 81 W smooth pipe, (b) 81 W grooved pipe, (c) 101 W smooth pipe, and (d) 101 W grooved pipe. These results reveal important insights into the impact of surface modifications on thermal performance and heat dissipation behavior. At a heat input of 81 W, the maximum wall temperature (the highest value on the contour scale) in the smooth pipe reached 376.1 K, localized near the heating interface. In contrast, the grooved configuration exhibited a peak temperature of 373.5 K, representing a temperature drop of 2.6 K. This reduction can be attributed to the improved heat transfer facilitated by the annular grooves. The enhanced surface area and locally higher liquid superheat promotes earlier bubble nucleation and more vigorous phase change, effectively lowering the wall temperature. When the heat input was increased to 101 W, the distinction between the two configurations became more pronounced. The smooth pipe peaked at 381.9 K, while the grooved pipe stabilized at 377.6 K, resulting in a 4.3 K reduction in peak temperature. This increasing temperature differential with higher thermal load underscores the superior heat dissipation capability of the grooved surface. The grooves support more uniform and distributed boiling, mitigating thermal hotspots and promoting effective vapor evacuation from the evaporator section. The thermal advantages of the grooved geometry

are further corroborated by corresponding changes in the vapor volume fraction (discussed in Section 4.1), where a consistent increase from 12.1% to 18.6% was observed in grooved pipes compared to their smooth counterparts. This enhanced vapor generation directly correlates with improved latent heat utilization and faster energy transport toward the condenser. These combined thermal effects lead to three notable improvements in heat pipe performance: a reduction in the peak (hot-spot) wall temperature by 2.6–4.3 K, which reduces the local thermal load on the wall but, as shown in Section 4.6, does not lower the overall thermal resistance; an increase in vapor fraction by 12.1–18.6%, indicating more intense phase-change activity and improved heat transport efficiency; and a faster onset and propagation of boiling, which facilitates quicker energy redistribution along the pipe and enhances cooling performance at the condenser end. The improved thermal profiles in grooved pipes indicate a more homogeneous temperature distribution, reduced local overheating, and superior boiling regulation. These outcomes are crucial for systems requiring stable and high-rate heat removal, such as concentrated solar thermal collectors, compact heat exchangers, and electronic cooling modules. From a physical perspective, the grooves function as both thermal and hydrodynamic enhancers. They increase the local wetted perimeter, which boosts convective heat transfer, and create geometric pockets of locally higher liquid superheat where vapor forms. Furthermore, the unsteady liquid motion produced by bubble growth and departure, which the model resolves, disrupts the thermal boundary layer and improves energy transport within the liquid.

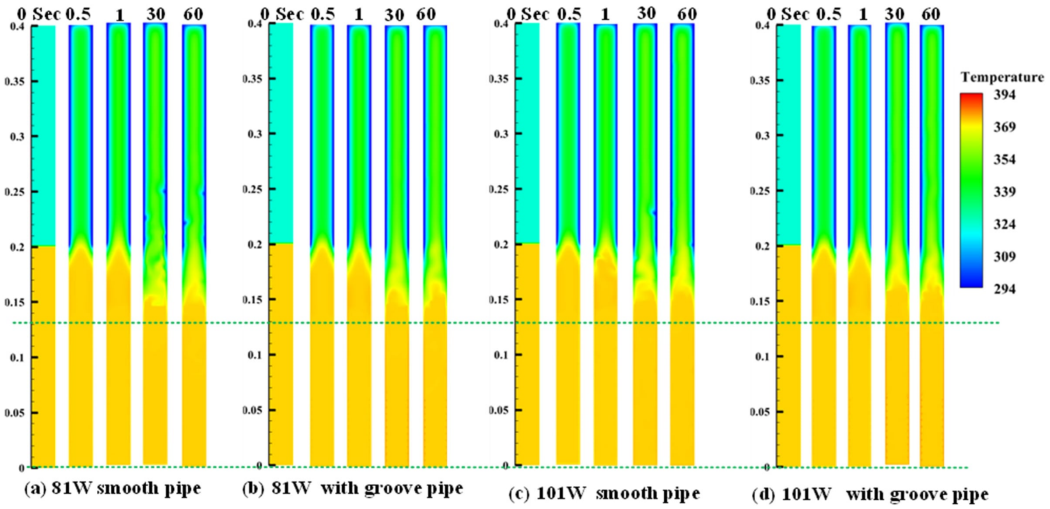


Figure 6. Temperature contours at for various computational times with heat inputs of 81 W and 101 W, illustrating the differences between smooth and grooved heat pipes.

In Figure 6 all contours use a common temperature range with magnified insets of the groove region, so that the local differences between the smooth and grooved pipes can be read directly. The peak values quoted above are hot-spot values on the contour scale near the heating interface. They are not the quantities in Figure 4 (steady axial wall-temperature profile, about 375 K over the evaporator for the smooth pipe at 101 W) or Figure 9 (time history of the heater temperature), which are averaged.

4.3. Bubble Dynamics and Nucleation Behavior at Low Heat Input

Figure 7 presents a comparative visualization of bubble evolution within the evaporator region of smooth and grooved heat pipe configurations under a constant heat input of 81 W. The temporal and spatial progression of vapor bubble nucleation, growth, coalescence, and transport provides key insights into the role of surface geometry on two-phase flow dynamics and thermal regulation. In the smooth pipe configuration (Figure 7a), nucleation

initiates once sufficient wall superheat develops, leading to bubble formation and upward migration toward the centerline. Small vapor bubbles rapidly detach from the heated surface and migrate toward the pipe's centerline, where they coalesce into larger vapor structures. This process results in a relatively uniform vapor plume, promoting unobstructed upward vapor transport. The smooth surface geometry reduces frictional resistance and enables continuous vapor escape along the axial direction, thereby supporting efficient latent heat removal.

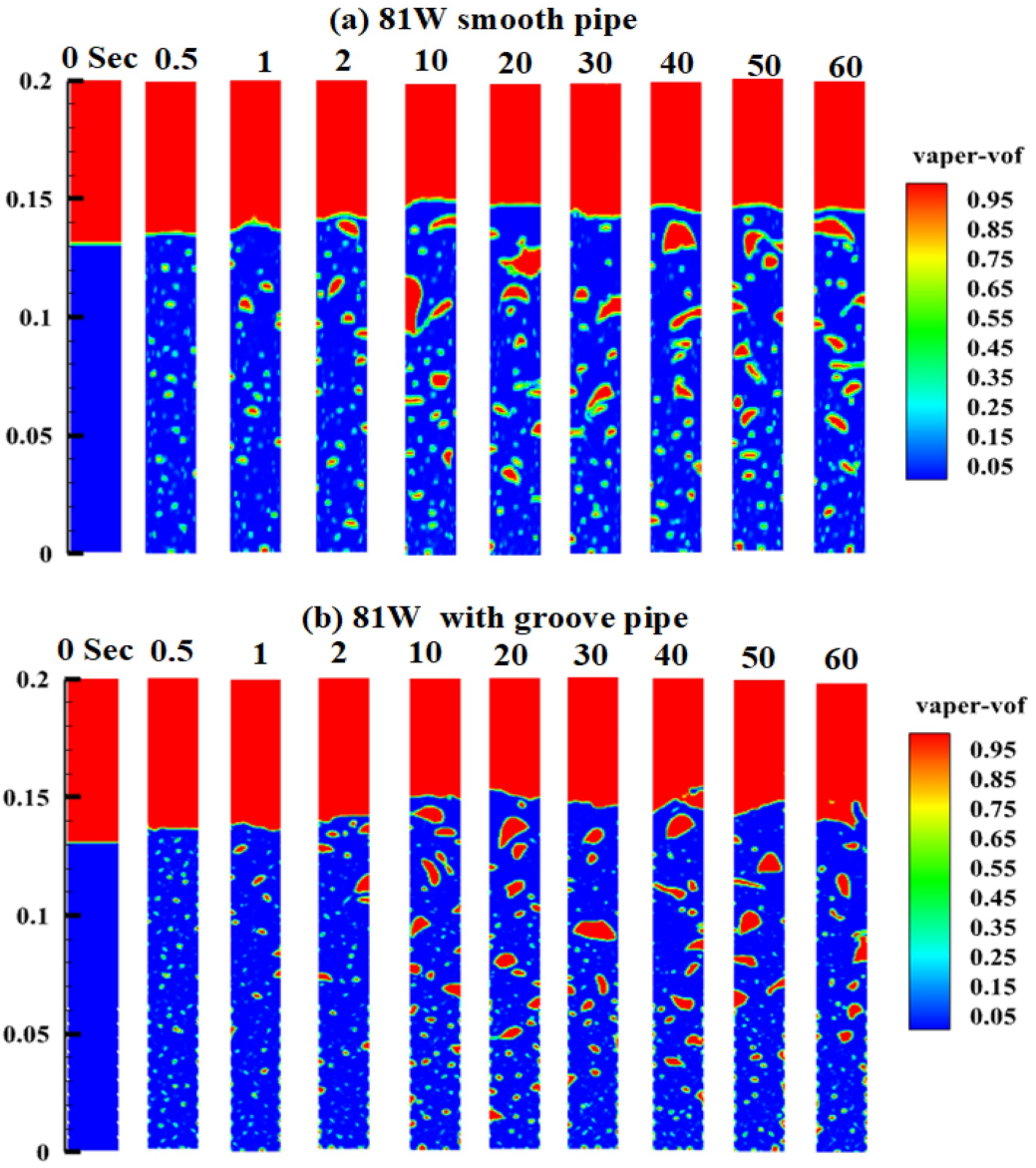


Figure 7. Bubble dynamics at different time steps for 81 W heat input: (**a**) smooth pipe, (**b**) grooved pipe.

In contrast, the grooved pipe configuration (Figure 7b) exhibits a markedly different bubble dynamic profile. The grooved configuration exhibits earlier visual nucleation due to additional micro-cavities serving as activation sites; however, the exact timing cannot be determined quantitatively. The number of active nucleation sites is afforded by the groove-induced surface roughness. However, the grooves also create localized capillary wells that encourage vapor entrapment. As a result, many bubbles adhere to the groove cavities rather than migrating immediately into the bulk flow. This leads to a higher density of vapor structures localized along the wall, with delayed coalescence and less organized upward motion. The grooves promote higher bubble retention along the wall, indicating longer

vapor residence time than in the smooth pipe surface, representing a 70% increase. This prolonged residence time indicates partial vapor entrapment within the groove structures, which, while beneficial for localized phase change, may introduce higher localized thermal resistance and delay vapor transport toward the condenser, particularly at low to moderate heat inputs.

This behavior reflects a dual-effect phenomenon in which grooves simultaneously enhance and limit thermal performance. On the other hand, the presence of grooves increases nucleation frequency and site density, promoting more active and widespread phase-change zones along the heated wall—an advantage particularly valuable in high heat flux applications requiring distributed boiling. On the other hand, these same grooves can impede bubble detachment and delay coalescence, resulting in localized vapor accumulation. This vapor crowding reduces convective replenishment of the liquid film and may increase thermal resistance, thereby partially offsetting gains in nucleation efficiency. From a physical standpoint, the grooved geometry provides enhanced microscale surface interactions, favoring early nucleation. However, the same structural features act as geometric constraints that influence bubble motion pathways. This interplay between surface-driven nucleation and confinement-induced entrapment defines the overall efficiency of the phase-change process in grooved systems. Therefore, while grooved surfaces demonstrate a higher nucleation site density and faster activation time, they also necessitate careful optimization of groove geometry, including spacing, depth, and orientation, to balance nucleation enhancement with bubble mobility and vapor evacuation. These findings emphasize the need for tailored surface micro-structuring based on operating heat flux and fluid properties to maximize thermal performance in heat pipe-based systems.

Bubble-dynamics metrics. Table 7 collects the quantitative results that were extracted from the bubble sequences of Figure 11 for the 101 W cases. Reducing the spacing from 10 to 5 mm raised bubble formation in the first 15 s by 27% and shortened the detachment interval from 4.5 s to 2.8 s, i.e., the departure frequency (the reciprocal of the interval) rose from 0.22 to 0.36 s^{-1}. Widening the grooves from 1.0 to 1.5 mm increased the number of active vapor sites at 20 s by 19% and lengthened the residence time of bubbles on the groove edges by a factor of 1.7. These quantities describe grid-resolved vapor structures and are comparative.

Table 7. Bubble-dynamics metrics from Figure 11.

Quantity	Change	Condition (101 W)
Bubble formation in the first 15 s	+27%	S: 10 → 5 mm (W = 1.0 mm)
Detachment interval	4.5 s → 2.8 s (−38%)	S: 10 → 5 mm (W = 1.0 mm)
Departure frequency (1/interval)	0.22 → 0.36 s^{-1} (+61%)	S: 10 → 5 mm (W = 1.0 mm)
Active vapor sites at 20 s	+19%	W: 1.0 → 1.5 mm (S = 5 mm)
Bubble residence time on groove edges	× 1.7	W: 1.0 → 1.5 mm (S = 5 mm)

Effect of the two-dimensional domain. In the planar model each bubble is a cylinder of infinite length, and vapor cannot spread around the circumference of an annular groove. Bubble shape, coalescence and residence time in three dimensions may differ, so the bubble-scale results are interpreted as trends between cases computed with the same model.

4.4. Bubble Dynamics at Elevated Heat Input (101 W): Influence of Surface Microstructure

Figure 8 compares the evolution of bubble dynamics at various time steps in smooth and grooved heat pipe configurations subjected to a higher heat input of 101 W. The results emphasize the pivotal role of surface morphology in dictating two-phase flow behavior under intensified thermal loading. In the smooth pipe (Figure 8a), the elevated heat flux accelerates nucleation, causing vapor bubbles to form rapidly along the heated wall.

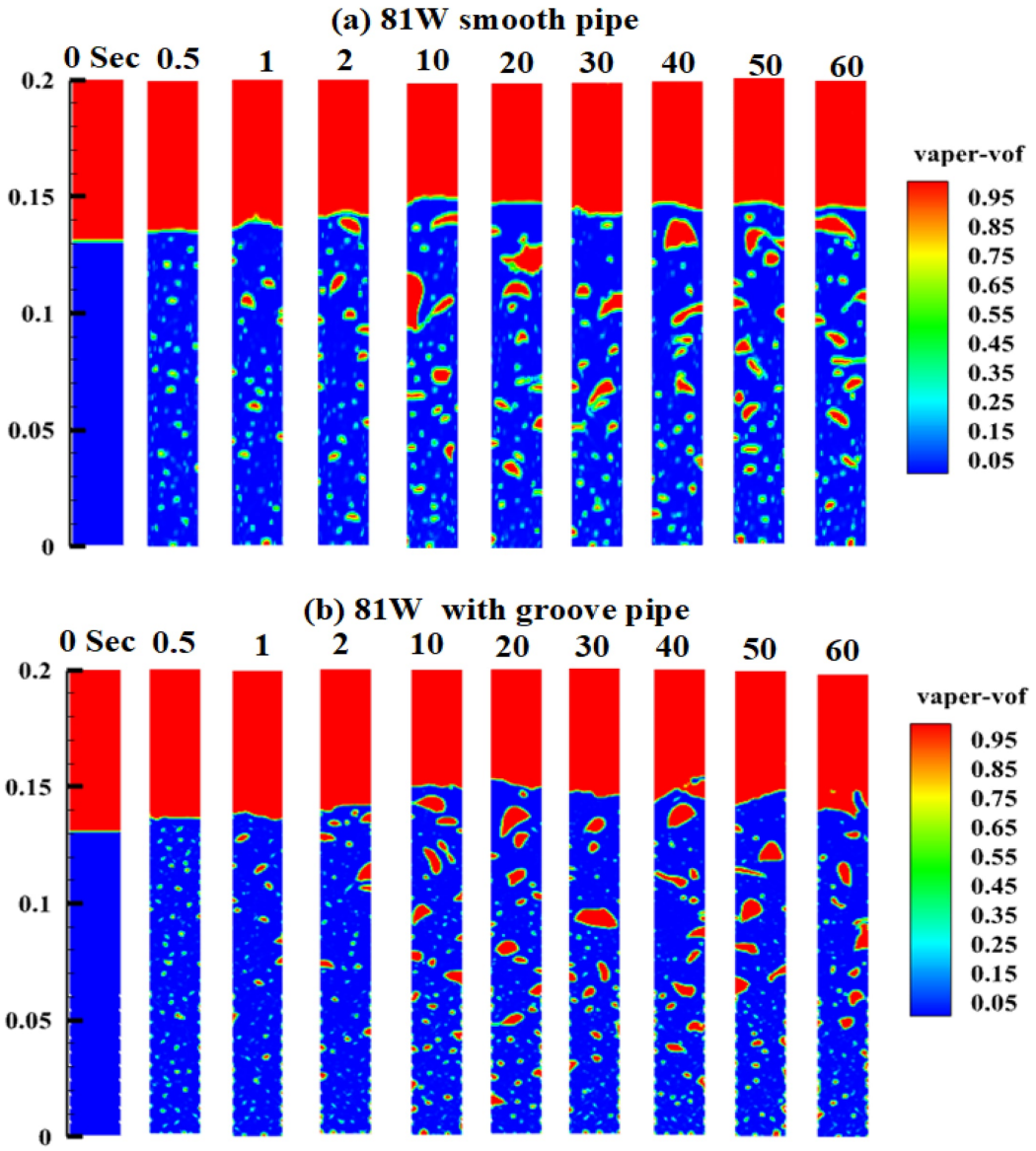


Figure 8. Bubble dynamics at different time steps for a heat input of 101 W: (**a**) smooth pipe, (**b**) grooved pipe.

At higher heat input, the smooth pipe exhibits rapid bubble growth and efficient coalescence into larger vapor structures that rise freely into larger vapor columns along the pipe centerline, facilitating unobstructed upward flow and swift vapor removal from the evaporator The dominant mechanisms here are bubble coalescence and axial streaming, which support effective thermal regulation through low-resistance vapor transport. Conversely, the grooved pipe (Figure 8b) exhibits markedly different dynamics. The increased surface area and micro-cavity action lead to earlier and denser nucleation. The grooved pipe exhibits denser nucleation activity, with more bubbles forming along the heated area than the smooth pipe, based on simulation frame analysis. However, several bubbles remain

attached to the groove cavities for extended periods, delaying coalescence, release, and axial transport. The grooves, while enhancing nucleation, also act as partial flow barriers, increasing local vapor residence time.

Despite this localized entrapment, overall vapor generation is higher in the grooved pipe than in the smooth pipe (a 12.1% improvement in average vapor fraction), indicating stronger boiling enhancement at elevated heat flux. This indicates that, under high heat input conditions, the advantages of intensified boiling due to groove-induced nucleation outweigh the drawbacks of vapor confinement. These findings indicate a heat-flux-dependent performance trade-off, where the impact of grooves varies with thermal loading. At lower heat inputs, grooves may marginally increase thermal resistance due to vapor entrapment and delayed bubble detachment. However, as heat input rises, the benefits of groove-induced nucleation become more pronounced, leading to enhanced vapor generation and lower local wall temperatures. Consequently, grooved surfaces may be advantageous for local hot-spot control at high heat flux, where the ability to maximize nucleation density and phase-change activity outweighs the drawbacks of localized vapor confinement.

Figure 9 shows the time history of the heater temperature and of the evaporator-section vapor fraction for the smooth and grooved pipes at (a) 81 W and (b) 101 W. At 81 W the smooth pipe has the higher vapor fraction during the first 10–20 s (about 0.14 at 10 s against about 0.11 for the grooved pipe), consistent with the initial bubble entrapment in the grooves. After about 30 s the grooved pipe is higher (about 0.105 against 0.089 at 40 s, i.e., about 18%, and about 10% on average over 30–60 s). At 101 W the grooved pipe is higher from about 10 s on (about 0.151 against 0.127 at 40 s, i.e., about 19%, and about 12% on average over 10–60 s). The heater temperature settles at about 362.8 K (smooth) and 363.9 K (grooved) at 81 W, and at about 364.0 K and 365.2 K at 101 W, i.e., about 1.1–1.2 K higher with grooves. This agrees with the slightly higher thermal resistance of the grooved pipe (Section 4.6), and it differs from the lower hot-spot temperature of the grooved pipe in Figure 6 (Section 4.2), because the heater temperature is an averaged quantity whereas the values presented in Figure 6 are local maxima. This transient behavior confirms the dual role of grooves: they initially delay vapor escape due to trapping but ultimately raise vapor production.

4.5. Geometric Effect on Vapor Fraction

Figure 10 examines the influence of groove geometry—specifically spacing and width—on the transient vapor fraction and heater wall temperature of a grooved heat input of 101 W. The results demonstrate that groove configuration plays a critical role in governing phase-change dynamics and thermal regulation.

Reducing the groove spacing from 10 mm to 5 mm increased the evaporator vapor fraction at 40 s slightly, from about 0.147 to 0.152 (Figure 10a), whereas the closest spacing of 2.5 mm gave a lower value (about 0.135); the heater temperature differed by 0.2 K or less between the three spacings (Figure 10b). The more frequent bubble formation and the shorter detachment interval at S = 5 mm (Section 4.4, Figure 11) are consistent with this small gain. Conversely, increasing the groove width from 1.0 mm to 1.5 mm gave a higher vapor-fraction peak (about 0.177 against 0.143 at 30 s) but not a consistently higher value (about 0.140 against 0.148 at 40 s; Figure 10c), and the width of 0.5 mm gave about 0.142 at 40 s with the lowest heater temperature (Figure 10d; differences below 0.2 K). Although wider grooves offer a greater surface area for nucleation and allow for the growth of larger vapor structures, they can also prolong bubble residence time within the groove cavities, leading to intermittent vapor trapping and thermal non-uniformities. The findings suggest that while both spacing and width influence boiling behavior, groove spacing has a more pronounced effect on bubble formation and departure. Over the tested range, however,

the differences in the evaporator vapor fraction (within about 3–13%) and in the heater temperature (0.3 K or less) between the cases are small, and the main effect of S and W is on the bubble behavior (Figure 11) rather than on these global quantities.

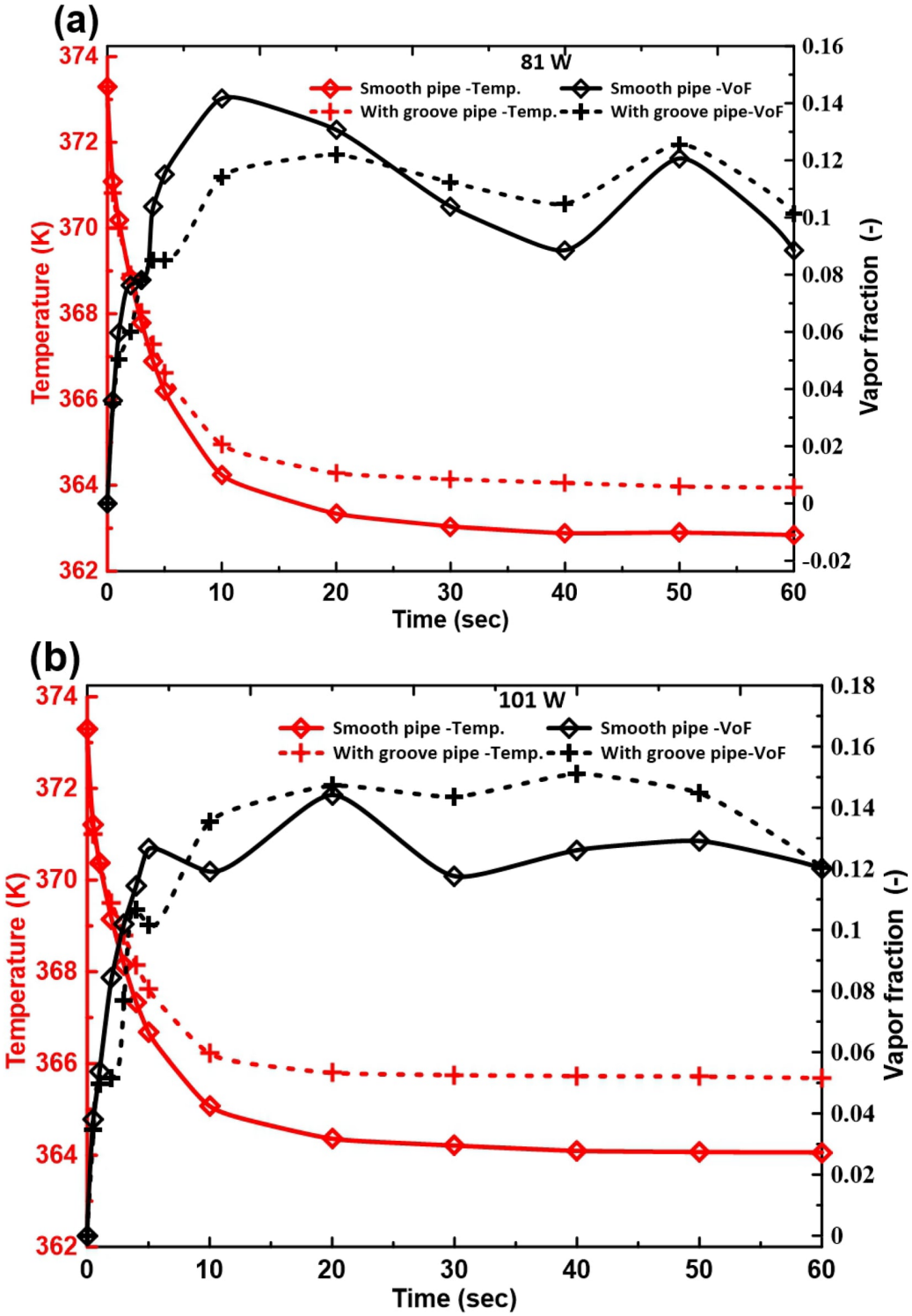


Figure 9. Transient variation in heater temperature and vapor fraction at the evaporator section: (**a**) 81 W heat input and (**b**) 101 W heat input.

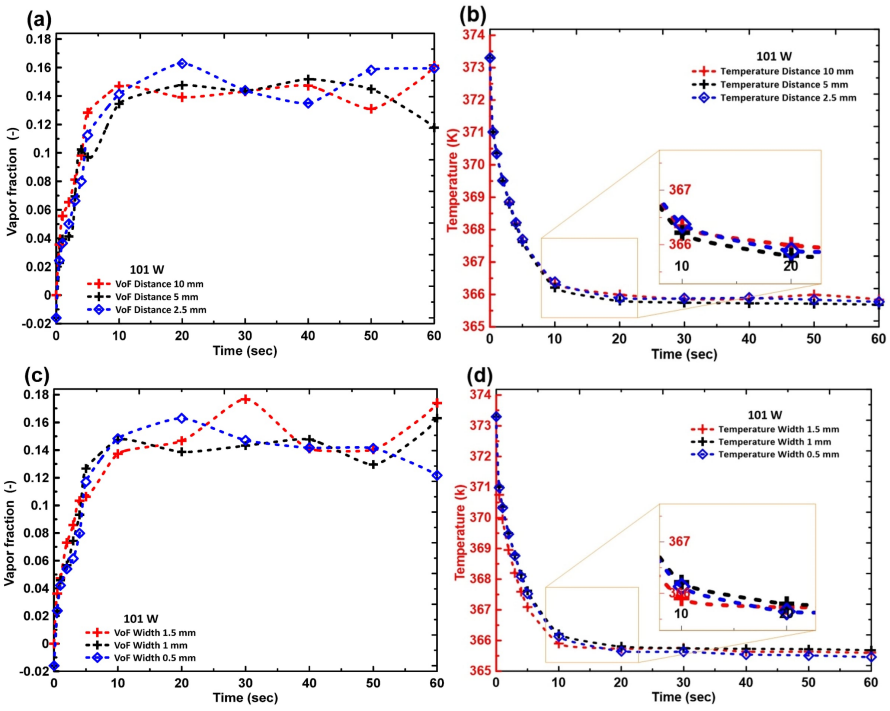


Figure 10. Transient variation of (**a**) vapor fraction at the evaporator section and (**b**) heater temperature of the grooved heat pipe at 101 W at different distances between grooves. (**c**) Vapor fraction at the evaporator section and (**d**) heater temperature of the grooved heat pipe at 101 W at different groove widths.

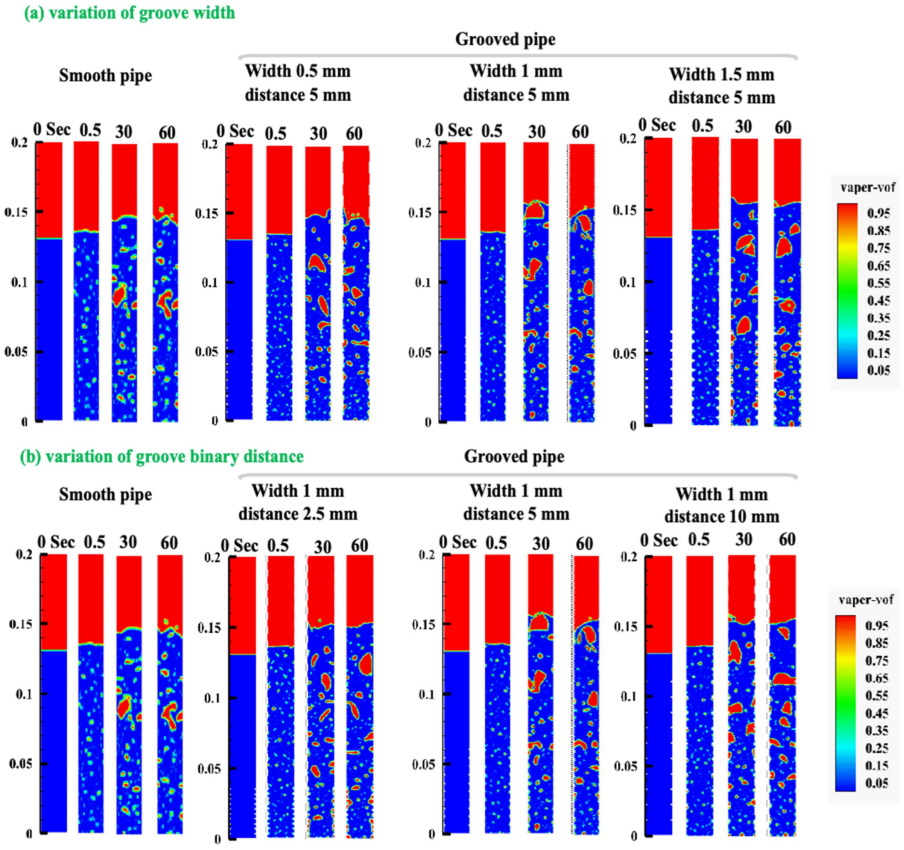


Figure 11. Bubble dynamics at different time steps for a heat input of 101 W: (**a**) Groove width variation. (**b**) Variation in groove spacing.

Figure 11 provides a detailed assessment of how groove geometry—specifically groove width and spacing, governs vapor bubble nucleation, growth, and detachment behavior under a constant heat input of 101 W, with direct implications for phase-change efficiency in grooved heat pipes. Increasing groove width from 1.0 mm to 1.5 mm resulted in a 19% rise in active nucleation sites at t = 20 s, highlighting the role of wider cavities in promoting localized boiling. However, this benefit is tempered by a 1.7-fold increase in bubble residence time along the groove edges, indicating that while wider grooves enhance nucleation, they also contribute to vapor retention and delayed detachment, which may hinder upward transport and reduce convective effectiveness. In contrast, decreasing groove spacing from 10 mm to 5 mm led to a 27% increase in bubble formation within the first 15 s and a 38% reduction in bubble detachment intervals—from 4.5 s to 2.8 s—indicating more vigorous and sustained boiling behavior. This tighter spacing increases nucleation site density and more frequent vapor release, promoting stronger transition boiling behavior and enhancing heat removal rates enhancing wall heat removal through intensified nucleation and more rapid bubble departure. Collectively, these results demonstrate that while both groove width and spacing strongly influence bubble dynamics, groove spacing plays a more decisive role in accelerating phase-change processes. The best groove design must therefore balance nucleation enhancement with vapor evacuation efficiency, as excessive vapor holdup or delayed detachment can offset thermal gains. These insights reinforce the importance of precisely engineered microgeometry in high-performance heat pipe systems, where fine-tuning of surface features directly impacts boiling intensity, flow structure, and overall thermal transport capability. Although localized vapor patches were observed at 101 W, a continuous, stable vapor film characteristic of film boiling was not detected. The boiling regime is therefore interpreted as intensified transition boiling rather than full film boiling.

Spacing-to-width ratio. The groove combinations simulated at 101 W were S = 10, 5 and 2.5 mm at W = 1.0 mm, and W = 0.5, 1.0 and 1.5 mm at S = 5 mm, i.e., S/W = 10, 5, 2.5, 10 and 3.3 (Table 8, from Figures 10 and 12). The overall thermal resistance varied by only about 0.5% among them (0.747–0.751 K W^{-1}), so it does not discriminate between them. The evaporator vapor fraction at 40 s was highest for S = 5 mm and W = 1.0 mm (S/W = 5). Together with the shorter detachment interval at S = 5 mm than at 10 mm and the shorter vapor residence at W = 1.0 mm than at 1.5 mm (Section 4.4), S = 5 mm and W = 1.0 mm (S/W = 5) is the best of the combinations tested. S/W alone does not determine the response (S/W = 10 occurs for two combinations with different vapor fractions), and S ≈ 5 mm appears to be the controlling parameter, with S/W of about 5–10 at that spacing as a suitable range. These values apply to the copper–water system at 65% filling ratio and 1.0 mm groove depth simulated here.

Table 8. Simulated groove combinations at 101 W (values read from Figures 10 and 12; precision about ±0.003 in vapor fraction, ±0.1 K and ±0.002 K W^{-1}).

S (mm)	W (mm)	S/W	Vapor Fraction (40 s)	Heater T (40 s, K)	R_{th} (K W^{-1})
10	1.0	10	0.147	365.9	0.751
5	1.0	5	0.152	365.7	0.749
2.5	1.0	2.5	0.135	365.9	0.750
5	0.5	10	0.142	365.6	0.747
5	1.5	3.3	0.140	365.7	0.748

4.6. Thermal Resistance

Finally, overall thermal resistance is commonly used to describe the performance of a heat pipe [31,32]. A lower thermal resistance signifies improved system performance. The overall heat transfer rate is directly proportional to the effective temperature difference between the heat source at the evaporator and the heat sink at the condenser, and inversely proportional to the equivalent thermal resistance between them. It can be expressed as:

$$R_{th} = \frac{T_{e,avg} - T_{c,avg}}{Q_{in}} \quad (17)$$

Figure 12, The thermal resistance of the heat pipe at steady state tends to be higher at lower heat input values compared to higher heat inputs. This is primarily because the phase change process is less efficient at lower temperatures. Understanding this relationship can help in enhancing the performance of heat pipes under varying thermal conditions. When the heat input is low, the temperature gradient between the evaporator and condenser is smaller, resulting in weaker boiling and reduced vapor generation. This leads to higher thermal resistance because the heat-transfer mechanisms are not fully optimized. For the grooved pipe, the thermal resistance is slightly higher than for the smooth pipe. This is attributed to the grooves, which create additional surface area and localized pockets where bubbles can form and adhere. While grooves enhance local nucleation sites, they can also impede the smooth flow of vapor, thereby increasing thermal resistance. The trapped bubbles in the case of heat transfer, compared to a smooth pipe, where the vapor can flow more freely. These factors combined result in the observed differences in thermal resistance at varying heat inputs and between smooth and grooved heat pipes.

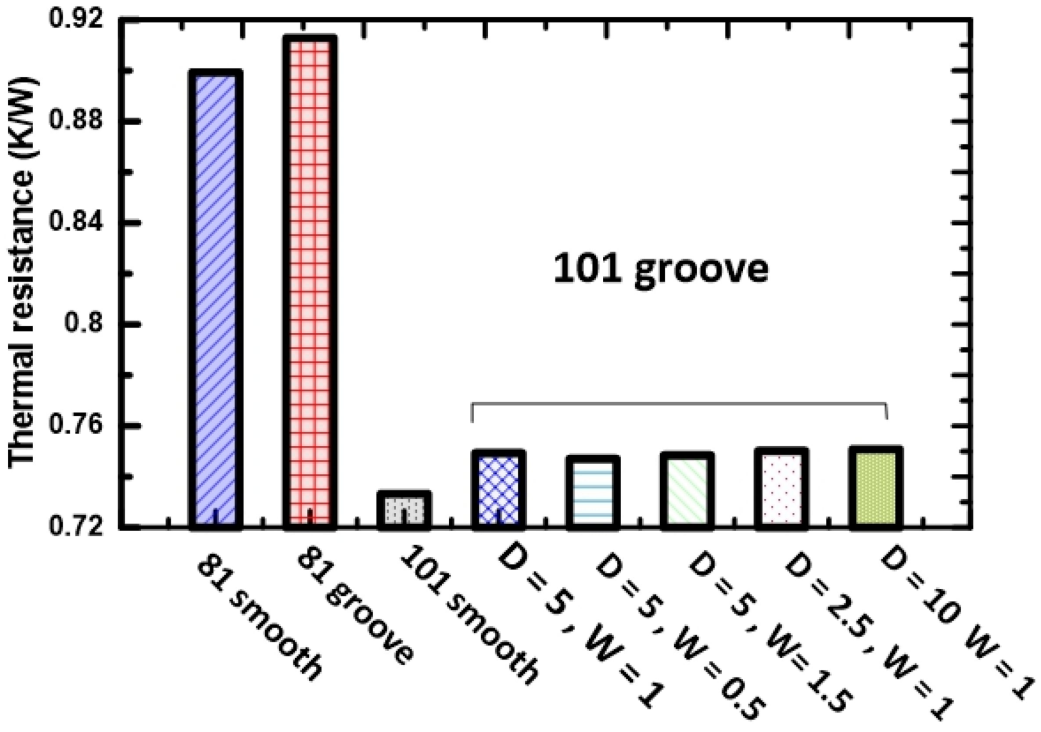


Figure 12. Thermal resistance with heat inputs of 81 W and 101 W for smooth and grooved heat pipes.

Local versus overall effect. Table 9 gives $R_{th} = (T_{e,avg} - T_{c,avg})/Q_{in}$ (Equation (17)), with *Te,avg* and *Tc,avg* the area-averaged wall temperatures of the evaporator and condenser, from Figure 12. The overall resistance of the grooved pipe is higher than that of the smooth pipe by about 1.4% at 81 W and 2.2% at 101 W, because retained vapor impedes departure, and R_{th} falls by about 18% for the smooth pipe when the heat input rises from 81 to 101 W.

Grooves lower the local peak wall temperature (2.6 K at 81 W and 4.3 K at 101 W) and raise vapor generation, but R_{th} uses area-averaged temperatures whereas the peak is a local hot-spot value; local boiling enhancement should therefore not be read as lower overall thermal resistance. The absolute R_{th} values depend on the condenser cooling and heat-loss treatment, so the comparison with [16,17] is limited to the trend that *Rth* falls with increasing heat input. For context, the Rohsenow pool-boiling correlation [49] and the thermosyphon correlation of Imura et al. [50] give evaporator coefficients of about 1.8 and 2.1 kW m^{-2} K^{-1} and about 3.3 and 3.6 kW m^{-2} K^{-1} at 81 and 101 W, i.e., wall superheats of about 3.6–3.8 K and 1.9–2.2 K (water properties at 373.15 K, Csf = 0.013, inner-wall flux). The smooth-pipe evaporator wall in Figure 4 is only about 1.5 K above T_{sat}, so the model probably over-predicts the evaporation coefficient, which is consistent with the under-predicted evaporator wall temperature in Section 3.1. The simulated heat inputs are far below the counter-current flooding limit (about 2.0 kW, Wallis form [51] with Cw = 1 and the 20.2 mm bore) and the Zuber critical heat flux (about 14 kW, [52]) estimated for this tube, and no dry-out was observed in the vapor-fraction contours.

Table 9. Thermal resistance, R_{th} (K W^{-1}), read from Figure 12 (±0.002 K W^{-1}).

Configuration	81 W	101 W
Smooth	0.899	0.733
Grooved (S = 5 mm, W = 1.0 mm)	0.912	0.749
Change due to grooves	+1.4%	+2.2%

5. Conclusions

This study used a transient two-dimensional VOF model with a temperature-driven Lee-type UDF, validated for a smooth copper–water thermosyphon, to examine annular grooves at 81 W and 101 W. The main findings are as follows:

(1) Grooves lowered the peak (hot-spot) evaporator wall temperature by 2.6 K at 81 W and 4.3 K at 101 W and raised the average vapor fraction by 12.1–18.6%.
(2) Reducing the groove spacing from 10 to 5 mm increased bubble formation in the first 15 s by 27% and shortened the detachment interval by 38% (4.5 s to 2.8 s).
(3) Wider grooves increased the number of wall-attached vapor sites by 19% but lengthened vapor residence by up to 70%, i.e., increased vapor retention, particularly at low heat input.
(4) These local gains did not give lower overall thermal resistance in all cases: R_{th} of the grooved pipe was about 1.4% (81 W) and 2.2% (101 W) higher than that of the smooth pipe (Table 9).
(5) Within the tested set, the best combination was S = 5 mm and W = 1.0 mm (S/W = 5), with S/W of about 5–10 at S = 5 mm as a design window; no universal optimum is claimed.

Design recommendations. (i) Consider annular grooves where the local hot-spot temperature matters at high flux (above about 6–7 kW m^{-2}), noting that the overall thermal resistance rose by 1.4–2.2% in the present simulations and that at 81 W the benefit was small. (ii) Prefer a spacing of about 5 mm or less and keep the width at or below 1.0 mm to limit vapor trapping. (iii) Keep the grooved length within the liquid pool so that all grooves are wet (65% fill in this study). (iv) Select S/W of about 5–10 at S ≈ 5 mm, and avoid wide, deep grooves that hold vapor. (v) Check the manufacturing limits on depth against wall thickness. (vi) Verify experimentally before use, because the grooved results are not directly validated and the model is 2D and laminar.

Author Contributions: Conceptualization, S.M.A.R. and E.M.A.Z.; Methodology, S.M.A.R.; Software, S.I. and E.M.A.Z.; Validation, S.M.A.R., S.I. and E.M.A.Z.; Formal analysis, S.M.A.R., S.I. and E.M.A.Z.; Investigation, S.M.A.R., S.I. and E.M.A.Z.; Data curation, S.I. and E.M.A.Z.; Writing—original draft, S.M.A.R., S.I. and E.M.A.Z.; Writing—review & editing, A.A.H., M.E.H.A., M.H. and A.M.R.; Visualization, S.M.A.R., A.A.H., M.E.H.A., M.H. and A.M.R.; Supervision, S.M.A.R.; Project administration, S.M.A.R. All authors have read and agreed to the published version of the manuscript.

Funding: This research received no external funding.

Data Availability Statement: The original contributions presented in the study are included in the article, further inquiries can be directed to the corresponding author.

Conflicts of Interest: The authors declare no conflict of interest.

Nomenclature

Symbols: C curvature (m^{-1}); Co Courant number; c_p specific heat (J kg^{-1} K^{-1}); D_o, D_i outer and inner diameter (m); E energy (J kg^{-1}); F_{CSF} surface-tension force (N m^{-3}); g gravity (m s^{-2}); h_c condenser coefficient (W m^{-2} K^{-1}); h_{fg} latent heat (J kg^{-1}); k thermal conductivity (W m^{-1} K^{-1}); $\dot{m}$ mass-transfer rate (kg m^{-3} s^{-1}); p pressure (Pa); Q heat input (W); R_{th} thermal resistance (K W^{-1}); S groove spacing (mm); S_m, S_E mass and energy sources; T temperature (K); t time (s); u velocity (m s^{-1}); W groove width (mm); α volume fraction; β relaxation coefficient (s^{-1}); μ viscosity (Pa s); ρ density (kg m^{-3}); σ surface tension (N m^{-1}). Subscripts: L liquid; V vapor; sat saturation; e, c evaporator, condenser. Vectors and tensors are in bold; scalars in italics.

References

1. Farjana, S.H.; Huda, N.; Mahmud, M.P.; Saidur, R. Solar process heat in industrial systems—A global review. *Renew. Sustain. Energy Rev.* **2018**, *82*, 2270–2286. [CrossRef]
2. Gil, J.D.; Topa, A.; Álvarez, J.; Torres, J.; Pérez, M. A review from design to control of solar systems for supplying heat in industrial process applications. *Renew. Sustain. Energy Rev.* **2022**, *163*, 112461. [CrossRef]
3. Bouziane, H.; Benhamou, B. Assessment of the impact of thermal energy storage operation strategy on parabolic trough solar power plant performance. *Renew. Energy* **2023**, *202*, 713–720. [CrossRef]
4. Ma, L.; Lu, Z.; Zhang, J.; Liang, R. Thermal performance analysis of the glass evacuated tube solar collector with U-tube. *Build. Environ.* **2010**, *45*, 1959–1967. [CrossRef]
5. Aggarwal, S.; Kumar, R.; Lee, D.; Kumar, S.; Singh, T. A comprehensive review of techniques for increasing the efficiency of evacuated tube solar collectors. *Heliyon* **2023**, *9*, e15185. [CrossRef] [PubMed]
6. He, Z.; Ge, H.; Jiang, F.; Li, W. A comparison of optical performance between evacuated collector tubes with flat and semicylindric absorbers. *Sol. Energy* **1997**, *60*, 109–117. [CrossRef]
7. Liu, C.; Zhang, Z. Thermal response of wall implanted with heat pipes: Experimental analysis. *Renew. Energy* **2019**, *143*, 1687–1697. [CrossRef]
8. Zhang, Z.; Liu, Q.; Yao, W.; Zhang, W.; Cao, J.; He, H. Research on temperature distribution characteristics and energy saving potential of wall implanted with heat pipes in heating season. *Renew. Energy* **2022**, *195*, 1037–1049. [CrossRef]
9. Samanci, A.; Berber, A. Experimental investigation of single-phase and two-phase closed thermosyphon solar water heater systems. *Sci. Res. Essays* **2011**, *6*, 688–693.
10. Faghri, A. *Heat Pipe Science and Technology*; Global Digital Press: Delaware, DE, USA, 1995.
11. Pietrasanta, L.; Postorino, G.; Perna, R.; Mameli, M.; Filippeschi, S. A pulsating heat pipe embedded radiator: Thermal-vacuum characterisation in the pre-cryogenic temperature range for space applications. *Therm. Sci. Eng. Prog.* **2020**, *19*, 100622. [CrossRef]
12. Min, W.; Zhong, W.; Yuan, Y.; Zhao, D.; Cao, X. Numerical simulation on heat transfer characteristics of a two-phase closed thermosyphon with low filling ratios. *Therm. Sci. Eng. Prog.* **2025**, *67*, 104165. [CrossRef]
13. Azzolin, M.; Mariani, A.; Moro, L.; Tolotto, A.; Toninelli, P.; Del Col, D. Mathematical model of a thermosyphon integrated storage solar collector. *Renew. Energy* **2018**, *128*, 400–415. [CrossRef]
14. Sadeghi, K.; Kahani, M.; Ahmadi, M.H.; Zamen, M. CFD Modelling and Visual Analysis of Heat Transfer and Flow Pattern in a Vertical Two-Phase Closed Thermosyphon for Moderate-Temperature Application. *Energies* **2022**, *15*, 8955. [CrossRef]
15. Ritthong, N.; Thongkom, S.; Sawisit, A.; Duangsa, B.; Ritthong, W. Optimization Design of Closed-Loop Thermosyphons: Experimentation and Computational Fluid Dynamics Modeling. *Energies* **2024**, *17*, 527. [CrossRef]
16. Alammar, A.A.; Al-Dadah, R.K.; Mahmoud, S.M. Numerical investigation of effect of fill ratio and inclination angle on a thermosiphon heat pipe thermal performance. *Appl. Therm. Eng.* **2016**, *108*, 1055–1065. [CrossRef]

17. Al Jubori, A.M.; Jawad, Q.A. Computational evaluation of thermal behavior of a wickless heat pipe under various conditions. *Case Stud. Therm. Eng.* **2020**, *22*, 100767. [CrossRef]
18. Yue, C.; Zhang, Q.; Zhai, Z.; Ling, L. CFD simulation on the heat transfer and flow characteristics of a microchannel separate heat pipe under different filling ratios. *Appl. Therm. Eng.* **2018**, *139*, 25–34. [CrossRef]
19. Höhne, T. CFD simulation of a heat pipe using the homogeneous model. *Int. J. Thermofluids* **2022**, *15*, 100163. [CrossRef]
20. Maghrabie, H.M.; Olabi, A.; Alami, A.H.; Al Radi, M.; Zwayyed, F.; Salamah, T.; Wilberforce, T.; Abdelkareem, M.A. Numerical simulation of heat pipes in different applications. *Int. J. Thermofluids* **2022**, *16*, 100199. [CrossRef]
21. Kalogirou, S.A.; Papamarcou, C. Modelling of a thermosyphon solar water heating system and simple model validation. *Renew. Energy* **2000**, *21*, 471–493. [CrossRef]
22. Xiang, J.; Chen, X.-B.; Huang, J.; Zhang, C.; Zhou, C.; Zheng, H. Thermal Performances Investigation of Anti-Gravity Heat Pipe with Tapering Phase-Change Chamber. *Energies* **2020**, *13*, 5036. [CrossRef]
23. Yu, C.-W.; Huang, C.S.; Tzeng, C.T.; Lai, C.-M. Effects of the Aspect Ratio of a Rectangular Thermosyphon on Its Thermal Performance. *Energies* **2019**, *12*, 4014. [CrossRef]
24. Lin, S.; Zhang, X.; Wu, H. Impact of axial gravity on the transport performance of an Ω-shaped axial groove heat pipe (Ω-AGHP): A numerical investigation. *Case Stud. Therm. Eng.* **2025**, *72*, 106179. [CrossRef]
25. Qu, J.; Guan, F.; Lv, Y.; Wang, Y. Experimental study on the heat transport capability of micro-grooved oscillating heat pipe. *Case Stud. Therm. Eng.* **2021**, *26*, 101210. [CrossRef]
26. Gou, X.; Zhang, Q.; Li, Y.; Liu, Y.; Liu, S.; Iram, S. Experimental Research on the Thermal Performance and Semi-Visualization of Rectangular Flat Micro-Grooved Gravity Heat Pipes. *Energies* **2018**, *11*, 2480. [CrossRef]
27. Lu, X.; Liu, J.; Tong, X.; Dai, R.; Xiao, Y.; Deng, J. Experimental investigation on thermal performance of gravity heat pipe with different pipe configurations. *Case Stud. Therm. Eng.* **2025**, *65*, 105695. [CrossRef]
28. Zhou, W.; Chen, Y.; Li, Y.; He, J.; Liu, Y.; Gao, J.; Jian, Y.; Liang, H. Experimental study on improving the heat transfer performance of large-diameter thin flattened heat pipes. *Case Stud. Therm. Eng.* **2024**, *61*, 105159. [CrossRef]
29. Wang, J. Experimental investigation of the transient thermal performance of a bent heat pipe with grooved surface. *Appl. Energy* **2009**, *86*, 2030–2037. [CrossRef]
30. Mukherjee, A.; Chakraborty, A.; Srivastava, P.; Singh, A. A numerical simulation of turbulent flow characteristics through periodic grooves of varying curvatures. *Sādhanā* **2024**, *49*, 106. [CrossRef]
31. Saygan, S.; Akkus, Y.; Dursunkaya, Z.; Cetin, B. Capillary boosting for enhanced heat pipe performance through bifurcation of grooves: Numerical assessment and experimental validation. *Int. Commun. Heat Mass Transf.* **2022**, *137*, 106162. [CrossRef]
32. McGlen, R.J. An introduction to additive manufactured heat pipe technology and advanced thermal management products. *Therm. Sci. Eng. Prog.* **2021**, *25*, 100941. [CrossRef]
33. Andrzejczyk, R. Experimental Investigation of the Thermal Performance of a Wickless Heat Pipe Operating with Different Fluids: Water, Ethanol, and SES36. Analysis of Influences of Instability Processes at Working Operation Parameters. *Energies* **2019**, *12*, 80. [CrossRef]
34. Liu, J.; Xie, G.; Simon, T.W. Turbulent flow and heat transfer enhancement in rectangular channels with novel cylindrical grooves. *Int. J. Heat Mass Transf.* **2015**, *81*, 563–577. [CrossRef]
35. Haque, M.R.; Hridi, T.J.; Haque, M.M. CFD studies on thermal performance augmentation of heat sink using perforated twisted, and grooved pin fins. *Int. J. Therm. Sci.* **2022**, *182*, 107832. [CrossRef]
36. Voigt, I.; Lütke, N.; Thüsing, K.; Winkler, M.; Drossel, W.-G. Development and Examination of an Internally Switchable Thermosiphon. *Energies* **2022**, *15*, 3891. [CrossRef]
37. Fadhl, B.; Wrobel, L.C.; Jouhara, H. Numerical modelling of the temperature distribution in a two-phase closed thermosyphon. *Appl. Therm. Eng.* **2013**, *60*, 122–131. [CrossRef]
38. Wang, X.; Liu, H.; Xue, Y.; Wu, N.; Gan, W.; Zhu, Y. Experimental and CFD investigation on the thermal performance of two phase closed thermosyphons: Effect of corrugated evaporator. *Appl. Therm. Eng.* **2024**, *257*, 124494. [CrossRef]
39. Magnabosco, A.; Fantin, D.; Gabellone, M.J.; Berto, A.; Bortolin, S.; Del Col, D. CFD-Based Design of Finned Surfaces for Enhanced Condensation Heat Transfer in a Grooved Heat Pipe. *Energies* **2026**, *19*, 960. [CrossRef]
40. Abdullahi, B. Development and Optimization of Heat Pipe Based Compound Parabolic Collector. Ph.D. Thesis, University of Birmingham, Birmingham, UK, 2015.
41. Jouhara, H.; Robinson, A.J. Experimental investigation of small diameter two-phase closed thermosyphons charged with water, FC-84, FC-77 and FC-3283. *Appl. Therm. Eng.* **2010**, *30*, 201–211. [CrossRef]
42. Yang, X.; Mühlhausen, M.-P.; Fröhlich, J. Interpolation methods for two-way coupled Euler-Lagrange simulation of finite-size bubbles. *Chem. Eng. Sci.* **2021**, *238*, 116566. [CrossRef]
43. Ansys, Inc. *Ansys Fluent Theory Guide 2023 R2*; Ansys, Inc.: Canonsburg, PA, USA, 2023.
44. Kurul, N.; Podowski, M.Z. Multidimensional effects in forced convection subcooled boiling. In Proceedings of the 9th International Heat Transfer Conference, Jerusalem, Israel, 19–24 August 1990; Volume 2, pp. 21–26.

45. De Schepper, S.C.K.; Heynderickx, G.J.; Marin, G.B. Modeling the evaporation of a hydrocarbon feedstock in the convection section of a steam cracker. *Comput. Chem. Eng.* **2009**, *33*, 122–132. [CrossRef]
46. Hirt, C.W.; Nichols, B.D. Volume of fluid (VOF) method for the dynamics of free boundaries. *J. Comput. Phys.* **1981**, *39*, 201–225. [CrossRef]
47. Brackbill, J.U.; Kothe, D.B.; Zemach, C. A continuum method for modeling surface tension. *J. Comput. Phys.* **1992**, *100*, 335–354. [CrossRef]
48. Lee, W.H. A pressure iteration scheme for two-phase flow modeling. In *Multiphase Transport: Fundamentals, Reactor Safety, Applications*; Veziroglu, T.N., Ed.; Hemisphere: Washington, DC, USA, 1980; Volume 1.
49. Rohsenow, W.M. A method of correlating heat-transfer data for surface boiling of liquids. *Trans. ASME* **1952**, *74*, 969–976. [CrossRef]
50. Imura, H.; Kusuda, H.; Ogata, J.; Miyazaki, T.; Sakamoto, N. Heat transfer in two-phase closed-type thermosyphons. *Trans. JSME* **1979**, *45*, 712–722.
51. Wallis, G.B. *One-Dimensional Two-Phase Flow*; McGraw-Hill: Detroit, MI, USA, 1969.
52. Zuber, N. *Hydrodynamic Aspects of Boiling Heat Transfer*; AEC Report AECU-4439; United States Atomic Energy Commission: Washington, DC, USA, 1959.

Disclaimer/Publisher's Note: The statements, opinions and data contained in all publications are solely those of the individual author(s) and contributor(s) and not of MDPI and/or the editor(s). MDPI and/or the editor(s) disclaim responsibility for any injury to people or property resulting from any ideas, methods, instructions or products referred to in the content.